The Relationship between Overshooting Tops in a Tornadic Supercell and Its Radar-Observed Evolution

HOWARD B. BLUESTEIN

School of Meteorology, University of Oklahoma, Norman, Oklahoma

DANIEL T. LINDSEY

NOAA/NESDIS, Fort Collins, Colorado

DANIEL BIKOS

Cooperative Institute for Research in the Atmosphere, Fort Collins, Colorado

DYLAN W. REIF AND ZACHARY B. WIENHOFF

School of Meteorology, University of Oklahoma, Norman, Oklahoma

(Manuscript received 17 May 2019, in final form 14 August 2019)

ABSTRACT

This is a study of a tornadic supercell in Kansas on 14 May 2018 in which data of relatively high spatiotemporal resolution from a mobile, polarimetric, X-band, Doppler radar were integrated with *GOES-16* geosynchronous satellite imagery, and with fixed-site, surveillance, S-band polarimetric Doppler radar data. The data-collection period spanned the early life of the storm from when it was just a series of ordinary cells, with relatively low cloud tops, through its evolution into a supercell with much higher cloud tops, continuing through the formation and dissipation of a brief tornado, and ending after the supercell came to a stop and reversed direction, produced another tornado, and collided with a quasi-linear convective system. The main goal of this study was to examine the relationship between the overshooting tops and radar observed features prior to and during tornadogenesis. The highest radar echo top was displaced about 10 km, mainly to the north or northeast of the main updraft and cloud top, from the supercell phase through the first tornado phase of the supercell phase, after which the updraft and the cloud top became more closely located and then jumped ahead; this behavior is consistent with what would be expected during cyclic mesocyclogenesis. The change in direction of the supercell later on occurred while the nocturnal low-level jet was intensifying. No relationship was apparent between changes in the highest cloud-top height and tornadogenesis, but changes in cloud-top heights (rapid increases and rapid decreases) were related to two phases in multicell evolution and to supercell formation.

1. Introduction

There are a number of observational studies of tornadogenesis in supercells using rapid-scan, ground-based, mobile Doppler radars that show tornadogenesis beginning at low levels and then advancing upward very rapidly (e.g., French et al. 2013; Houser et al. 2015; Bluestein et al. 2019). There are theoretical reasons why tornado formation should be a low-level process (Rotunno 2013): when a mesocyclone is situated near the boundary layer, frictionally induced convergence underneath it can act to amplify the vorticity close to the ground (Wicker and Wilhelmson 1995; Coffer and Parker 2015). For this reason tornadoes are strongest at low levels, and most Doppler radar studies have focused their attention on the lowest levels of a supercell to decrease the update time, at the expense of vertical coverage and especially what happens in upper portions of the storm (e.g., Kosiba et al. 2013; Bluestein et al. 2019).

Supplemental information related to this paper is available at the Journals Online website: https://doi.org/10.1175/MWR-D-19-0159.s1.

Corresponding author: Howard B. Bluestein, hblue@ou.edu

DOI: 10.1175/MWR-D-19-0159.1

Some theoretical and observational studies have implicated the role of downdrafts and high momentum transferred downward to the ground by downdrafts [e.g., as internal momentum surges (Marquis et al. 2008; Skinner et al. 2014; Bluestein et al. 2016; Schenkman et al. 2016)] or just descending air in general, in forming tornadoes (Eskridge and Das 1976; Fujita et al. 1976; Davies-Jones and Brooks 1993; Gaudet and Cotton 2006). It has been argued that downdrafts are necessary for getting vorticity to the surface and that localized convergence along the rear-flank gust front (RFGF) due to jets produced underneath downdrafts (e.g., Bluestein et al. 2003) could be responsible for producing vortices. Descending reflectivity cores (DRCs) (Rasmussen et al. 2006; Kennedy et al. 2007; Byko et al. 2009; Markowski et al. 2012; Bluestein et al. 2019), which might be associated with downdrafts, have been implicated in some instances of tornadogenesis. While it may be that downdrafts are due in large part to downward-directed pressure-gradient forces at low levels (Klemp and Rotunno 1983) and strong negative buoyancy due to evaporation and precipitation loading at low and midlevels (e.g., in, or melting at midlevels), it is not known to what extent collapsing, overshooting tops at the *summit* of the supercell may play a role in tornadogenesis through downdrafts initiated below them when they collapse. It might be that the downdrafts do not extend far enough down in the storm to have an effect on what happens in the boundary layer.

In addition, while low-level convergence in the boundary layer intensifies a surface vortex, it is not known how high up in the parent supercell the updraft extends. It is possible that an overshooting top may be connected to an updraft that extends continuously downward in the storm to the boundary layer so that it may be associated with tornadogenesis, or it may be associated with an updraft that is present only in the upper portion of the storm, or one that earlier was at lower altitude and moved upward. Tanamachi et al. (2012) documented a tornadic supercell in which a weak-echo hole (WEH) extended from near the ground all the way to the top of the storm. The WEH is evidence of strong rotation owing to the centrifuging of scatterers (e.g., Dowell et al. 2005) and possibly an updraft that advects air devoid of precipitation from the boundary layer up to the top of the storm as a weak-echo column (WEC) (Tanamachi et al. 2012).

The overall scientific question to be addressed in this study is therefore as follows: What is the relationship between storm-top-observed updrafts (the growth and collapse of overshooting/penetrating tops) and the wind, reflectivity, and polarimetric variables in the interior of a supercell, particularly when a tornado forms? With the advent of rapid-update geosynchronous satellites (Schmit et al. 2005, 2017; Line et al. 2016) and mobile and/or fixed-site rapid scan, (polarimetric) Doppler radars (Wurman and Randall 2001; Bluestein et al. 2010; Pazmany et al. 2013; Kurdzo et al. 2017), it is possible to begin to answer this question. Rapid updates are necessary because tornadoes evolve on time scales as short as ~10 s. Dworak et al. (2012) compared *GOES-12*-derived overshooting tops to WSR-88D data and found that overshooting tops often corresponded with the maximum reflectivity aloft and the highest radar echo top. However, their study utilized relatively coarse radar and satellite data in both space and time.

On 14 May 2018, a team from the University of Oklahoma (OU) collected mobile Doppler radar data at close range (<10–20 km) for ~3 h during the afternoon and early evening in south-central Kansas, during which time a series of multicell convective storms evolved into a supercell and eventually produced a small tornado. The main purpose of this paper is to describe the correlation between the location of the main updraft, as evidenced by visible and infrared satellite imagery of the highest cloud feature/penetrating top/overshooting top, radar features such a Z_{DR} column/ring (e.g., Kumjian and Ryzhkov 2008; Snyder et al. 2013; Wienhoff et al. 2018) and a bounded weak-echo region (BWER) (Lemon et al. 1978), and other internal, radar-observed storm features such a hook echo, inflow notch, and tornadic vortex signature (TVS) (Brown et al. 1978). This case study may be the first to correlate high-resolution satellite imagery with high-resolution, mobile, Doppler radar data. A secondary goal of this study is to document and explain convection initiation (CI) and convective-storm evolution in general. The main objectives of this study are met by integrating observations from a number of different types of observing systems.

A description of the radar and satellite data used in this study is given in section 2. Section 3 contains an overview of the storm evolution and its synoptic-scale and mesoscale environment and section 4 contains a description of the relationship between the satellite and radar-observed features. A summary and conclusions are found in section 5.

2. Data

The three main sources of data are the Rapid-scan X-band Polarimetric (RaXPol) mobile radar, visible and infrared imagery from the *GOES-16* satellite,

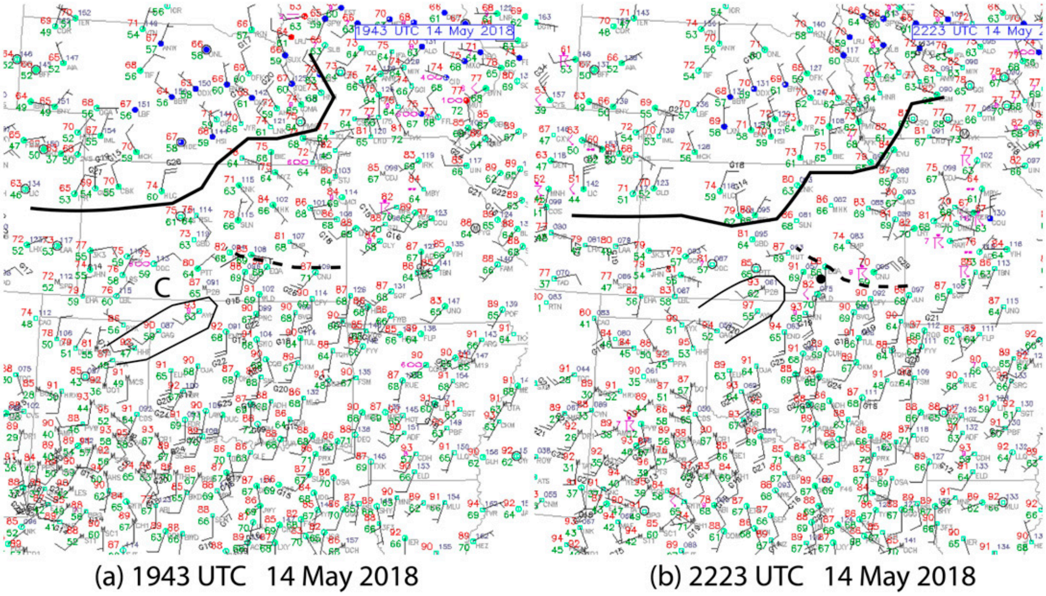

(a) 1943 UTC 14 May 2018 (b) 2223 UTC 14 May 2018

FIG. 1. Surface maps at (a) 1943 UTC 14 May 2018, approximately when storms were first initiated and at (b) 2223 UTC, just before multicells evolved into a supercell. Temperature (red) given in °F; dewpoint temperature (green) also given in °F. Winds plotted with half (full) barb indicating 2.5 (5) m s^{-1}. Cold front to the north indicated by solid black line; curved dashed line denotes location of outflow boundary. Corridor of relatively warm, dry air indicated by bulging black line. ''C'' indicates center of cyclone in (a); dot in (b) indicates approximate location of radar truck. (From UCAR/RAP.)

and WSR-88D S-band, polarimetric, Doppler radar data from Wichita, Kansas (KICT).

a. RaXPol data

Detailed technical information about RaXPol is found in Pazmany et al. (2013). RaXPol is an X-band, mobile radar that makes use of frequency hopping, a technique that allows for the collection of a sufficient number of independent samples for estimates of reflectivity, Doppler velocity, and polarimetric variables, despite the pedestal's rapid (as fast as 180° s^{-1}) mechanical rotation. The parabolic dish has a half-power width of 1°, which may be smeared to as much 1.4°–1.5° at the highest pedestal rotation speed. Volume scans were available every ~22 s during the time the storm was a supercell (>2304 UTC) (0°–20° elevation angle in increments of 2°) and every ~34 s prior to when the storm was a supercell (<2304 UTC) (0°–30° elevation angle in increments of 2°). Data were displayed and manually edited using the third version of SOLO (Oye et al. 1995).

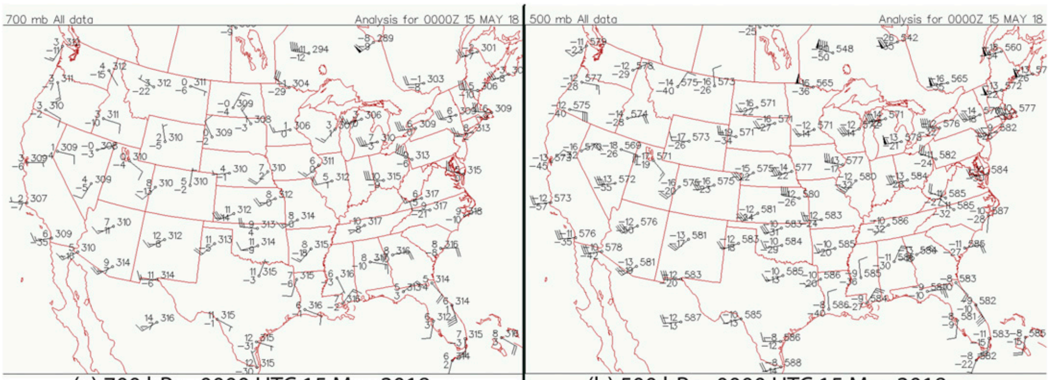

(a) 700 hPa 0000 UTC 15 May 2018 (b) 500 hPa 0000 UTC 15 May 2018

FIG. 2. Constant-pressure data maps for the contiguous United States at 0000 UTC 15 May 2018 at (a) 700 and (b) 500 hPa. Temperature in °C; dewpoint also in °C. Half (full) wind barbs indicate 2.5 (5) m s^{-1}. Height in dam. (From Plymouth State University.)

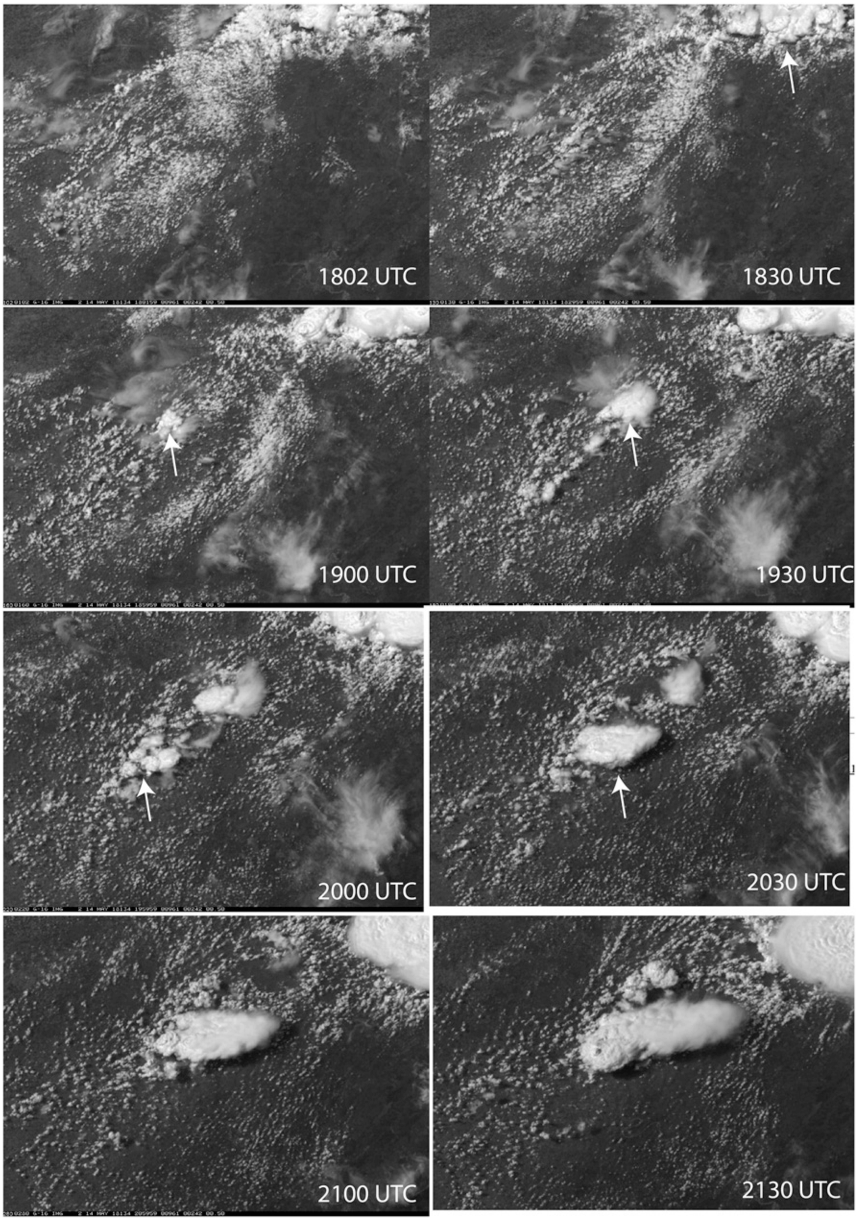

FIG. 3. *GOES-16* 0.64 μm visible satellite imagery every 30 min, from ~1800 UTC 14 May to 0300 UTC 15 May 2018 zoomed in on south-central Kansas, which show a developing multicell complex and its evolution into a supercell. Arrow at 1830 UTC points to convection along the outflow boundary in eastern Kansas. Arrows from 1900 to 2030 UTC point to the developing multicell storm. Arrows at 0000 and 0030 UTC point to left- and right-moving (LM, RM) splitting storms. (From NESDIS/CIRA/CSU.)

b. GOES-16 *data*

Detailed technical information on the *GOES-16*(R) geosynchronous satellite and its imager is found in Schmit et al. (2005, 2017). Imagery was available at 1-min intervals since one of the movable mesoscale domains was situated over the Oklahoma–Kansas region on the afternoon of 14 May 2018. The satellite pixel size at the latitude and longitude of the storm is 582 m × 775 m in the visible channel (0.64 μm) imagery and 2330 m × 3000 m in the infrared "window" channel (10.4 μm) imagery.

c. WSR-88D data from KICT

Standard, operational network WSR-88D data (Crum and Alberty 1993) were obtained from the National

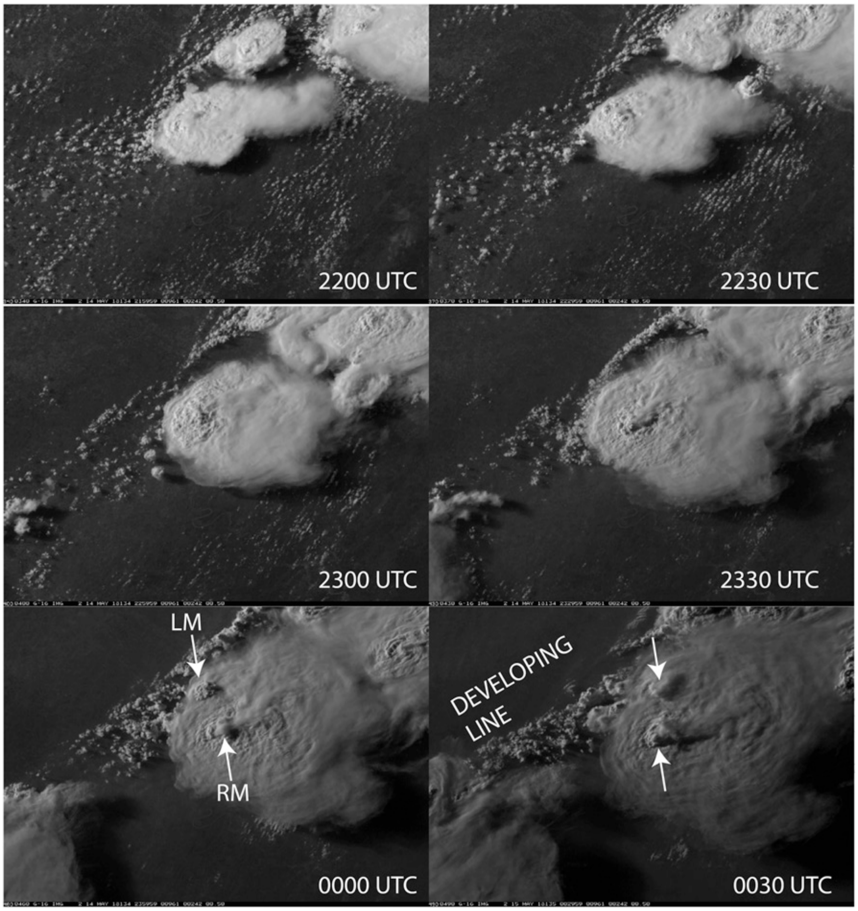

FIG. 3. (*Continued*)

Climatic Data Center (NCDC). Full volume scans were available every ~4.5 min using VCP (volume coverage pattern) (Crum et al. 1993; Brown et al. 2005) 212, which is similar to VCP 12, but with a different signal processing algorithm (SZ-2) for range folding mitigation. GridRad data (Cooney et al. 2018), which are a dataset made up of merged WSR-88D Level-2 data across most of the contiguous United States on a longitude–latitude–altitude grid with spacing of 0.02° × 0.02° × 1 km, every hour beginning at 0000 UTC each day, were used to estimate cloud-top height.

3. Overview of storm evolution and its mesoscale and synoptic-scale environment

a. *Surface features*

During the midafternoon (1943 UTC; CDT is 5 h earlier), warm, moist air covered central and eastern Oklahoma and far southeastern Kansas, where surface temperatures were ~86°–92°F (30°–33°C) and surface dewpoints were at least 68°F (20°C) in a plume that extended as far to the east as far eastern Oklahoma, but not all the way to the Arkansas border. The plume of warm, moist air flowing northward intersected an outflow boundary in southeastern Kansas, created by prior and ongoing convection in east-central and southeastern Kansas (Fig. 1a). An elongated surface cyclone was centered approximately between Dodge City (DDC) and the Oklahoma border. To the north of the cyclone, the winds were mainly from the northeast and the temperatures were mostly at or below 80°F (~27°C), while just to the southeast, in northwestern Oklahoma, there was a narrow, southwesterly, relatively hot (90°–93°F, 32°–34°C) and dry (dewpoints 47°–63°F, 8°–17°C) current of air directed toward the border between south-central Kanas and north-central Oklahoma. An even colder surface boundary (cold front) extended from northwestern Kansas to far southeastern Nebraska and up into western Iowa. Temperatures behind the cold front were as cool as the mid-60s °F (upper teens °C) and the winds had a northerly component.

By late in the afternoon (2223 UTC) the cold front to the northwest had progressed farther to the south and east, but temperatures were relatively cool ahead of it (only in the upper 70s to mid-80s F; 26°–30°C (Fig. 1b)). The outflow boundary in southeastern Kansas had strengthened, as the cold pool was more intense, owing to the ongoing convective storms in eastern Kansas. The warm, dry current of air that originated in northwestern Oklahoma now extended up into south-central Kanas.

b. *Synoptic-scale forcing*

Quasigeostrophic forcing was qualitatively weak at 0000 UTC 15 May, as evidenced by very weak temperature gradients at 500 and 700 hPa (Fig. 2): Since the temperature varied only 1°–2°C across Kansas and Oklahoma, and the geostrophic wind was relatively uniform, it follows that **Q**-vector convergence and vertical motion were weak. A trough/cyclone at 500 hPa was located over central California, Nevada, and Utah, far to the west of our area of interest.

c. *Convection initiation and storm environment*

Convective storms formed after cumulus congestus began appearing around 1900 UTC (Fig. 3) (see also the online supplemental file), along a northeast–southwest-oriented line, from south-central Kansas into north-central Oklahoma, along and just to the southeast of the hot, dry jet of air. It appears as if CI began along what looked like a northeast–southwest-oriented dryline, or possibly a dryline bulge (Koch and McCarthy 1982) (Fig. 1). There were no nearby soundings at the time of CI, but based on the Norman and Lamont soundings at 0000 UTC 15 May (Figs. 4a,c), and surface observations at 1943 UTC [Fig. 1a, a temperature of 92°F and dewpoint of 68°F (33° and 20°C, respectively), as was reported at Enid (END), which is ~40 km southwest of Lamont] surface-based CI was possible. The 0000 UTC Dodge City sounding had a much drier boundary layer (Fig. 4b), while the 0000 UTC Topeka, Kansas, sounding had a much weaker or nonexistent capping inversion at the top of the moist boundary layer (Fig. 4c), and was behind the outflow boundary (Fig. 1b). At Norman and Lamont the surface-to-6 km shear was too weak to support supercells, as the winds at 500 hPa were only around 7.5 and 15 $\mathrm{m\,s^{-1}}$, respectively, while to the north, in Kansas, the winds at 500 hPa at Topeka and Dodge City were approximately 20 $\mathrm{m\,s^{-1}}$, with a moderate westerly component (Fig. 4). The sfc–6 km vertical wind shear in Kansas was therefore ~20 $\mathrm{m\,s^{-1}}$ or more, sufficient for supercell formation, while in Oklahoma it was no more than ~10–15 $\mathrm{m\,s^{-1}}$, supportive of multicell convection. The CAPE at Norman was at least 2000 $\mathrm{J\,kg^{-1}}$, which is more than adequate for supercell formation.

The initial convective storms propagated toward an outflow boundary in southeast Kansas, under weak synoptic-scale forcing, but with marginal supercell shear in Kansas and subsupercell shear in Oklahoma. When RaXPol arrived at the scene of CI near the Kansas–Oklahoma border south of Wellington, KS, multiple convective towers appeared, dropped precipitation, and moved to the northeast, with their anvils streaming out (not shown), and their updraft bases on the western side of the visible precipitation cores (Fig. 5). A series of ordinary cells formed and all took similar tracks to the northeast (see supplemental animation). The radar crew did not follow any of the cells, but remained nearly stationary as long as the storms were within close range of the radar (<20 km) (Fig. 6); over a 3 h period, the radar moved only three times, one time which was only ~1 km.

d. *Storm evolution on the mesoscale*

Storm evolution on the mesoscale is depicted by imagery from the WSR-88D radar at Wichita, Kansas (KICT), which showed a series of small, ordinary cells (multicells), beginning at ~2000 UTC, just to the south and southwest of the Kansas border, in extreme north-central Oklahoma (Fig. 7a; see the satellite image in Fig. 3), and moving northeastward into Kansas and backbuilding (Bluestein and Jain 1985). Pulses of new convective cells kept on appearing near I-35, south of Wichita, particularly between 2106 and 2235 UTC, while the eastern edge of the radar echo progressed eastward. It is mainly for this reason that RaXPol was able to remain relatively fixed to one location; in addition, the early convective cells appeared to be weak and not worth following. At 2306 UTC the multicell storm consolidated into a more coherent radar echo and propagated eastward, away from I-35. At 2135 UTC, a fine line appeared southwest of Wichita, and persisted for several hours; it curved outward to the west, and while not visibly connecting to the storm to its southeast prior to 2319 UTC, when it became clearly connected to the hook echo which had formed, it is postulated that it was associated with outflow from the convective storms ongoing to the northeast and the new storm to the southeast, and connected to the back edge of the storm south/southeast of Wichita. The location of periodic new pulses of convection therefore appeared to be near the intersection of an outflow boundary, the jet of warm, dry air from the southwest, and warm, moist air from the south.

Between 2319 and 0105 UTC the storm, now a supercell (Fig. 7b), propagated to the southeast. At 2332 UTC, a cell split off on its northern flank, becoming a left mover, and continued to split from its parent, right-moving supercell (the mean wind was approximately from the west; Fig. 4). As the right mover crossed the Kansas–Oklahoma border at 0105 UTC, a broken-line squall line

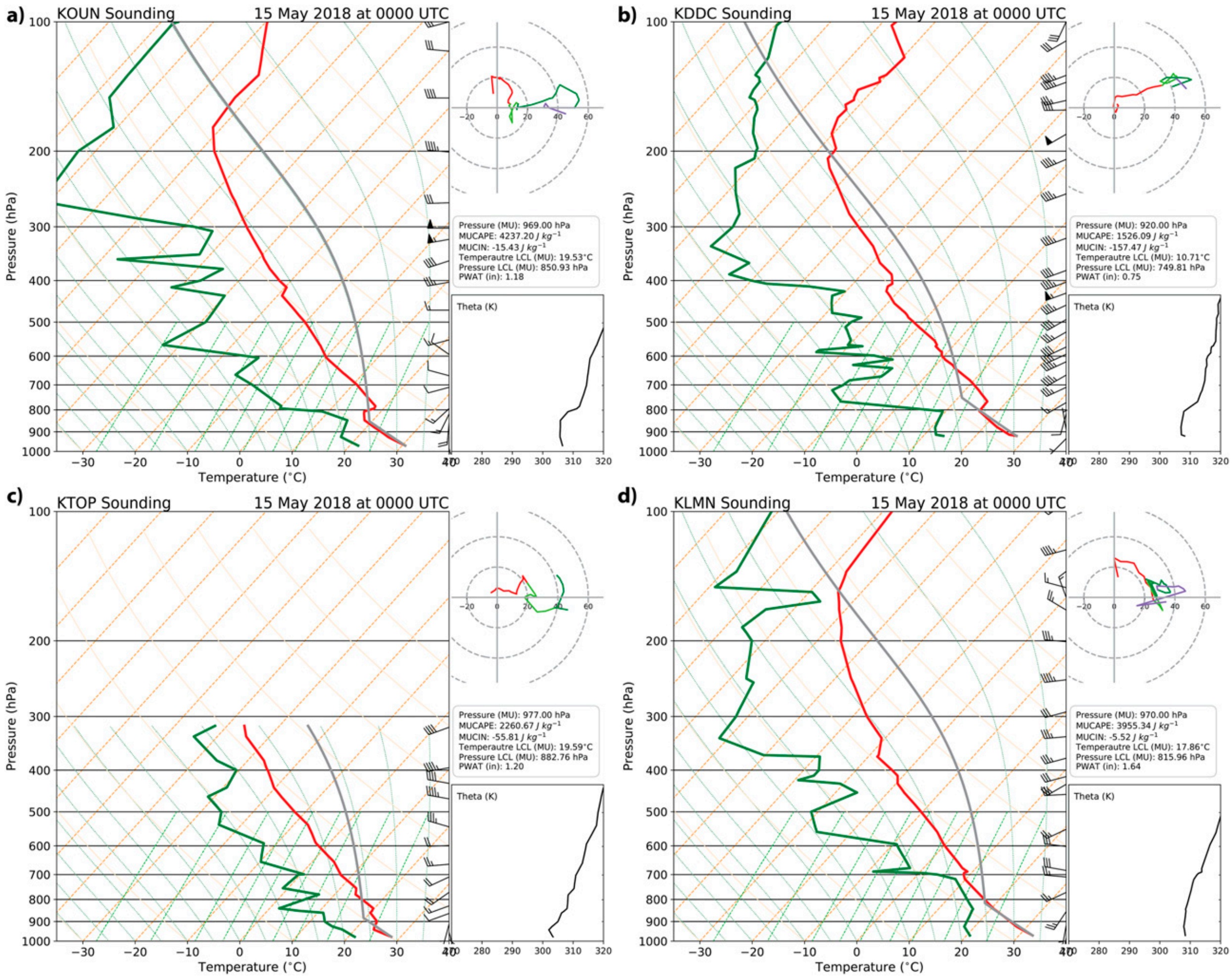

FIG. 4. Soundings (skew *T*–log*p* diagrams) at 0000 UTC 15 May 2018, for (a) Norman, OK, (b) Dodge City, KS, (c) Topeka, KS, and (d) Lamont, OK (in north central Oklahoma). Pressure given in hPa at the ordinate in a logarithmic scale; (a)–(c) temperature (red lines), dewpoint temperature (green lines), in °C. Winds plotted with half (full) barb indicating 2.5 (5) $\mathrm{m\,s^{-1}}$. (From UCAR/RAL and the University of Wyoming.)

(Bluestein and Jain 1985) began to form to its west, aligned in a northeast–southwest direction, along the cold front approaching from the northwest (not shown). By 0148 UTC (Fig. 7c), the supercell had stopped progressing any farther into Oklahoma and a well-defined northeast–southwest-oriented squall line now was positioned to the northwest of the supercell. At 0208 UTC, the supercell began propagating to the northeast, producing tornadoes at 0251 and 0320 UTC in south-central Kansas (*Storm Data*). At 0251 UTC, the supercell was still isolated, but after 0308 UTC it merged with the squall line, which had developed a bow echo around 0221 UTC; the merger occurred near the northern portion of the bow.

The evolution of the tornadic supercell therefore exhibited a wide variety of behavior, from classic multicell pulses and backbuilding to a discrete, isolated supercell with deviant motion; the sudden retreat of a right-moving supercell to the left, however, is unusual. This sudden change in direction could have been a result of the increase in the speed of the southerly low-level jet near and after sunset; between 0100 and 0200 UTC the hodograph based on data from NOAA's Rapid Refresh (RAP) system (Benjamin et al. 2016) displayed a well–defined south-southeasterly jet (nocturnal low-level jet; NLLJ) of around 36 $\mathrm{m\,s^{-1}}$; earlier, the mean wind in the lowest 3 km (red line in Fig. 8) was from the southwest, but more from the south-southwest at 0200 UTC. The wind speed at 1 km AGL from Doppler lidar data at the Southern Great Plains ARM site (Mather and Voyles 2013), nearby to the southwest, in Oklahoma, increased from the south from about 12.5 $\mathrm{m\,s^{-1}}$ at 0015 UTC to 20–22 $\mathrm{m\,s^{-1}}$ after 0000 UTC (Fig. 9a). The wind speed at 500 m, also at the ARM site, but from a Doppler radar 915 MHz wind profiler (Mather and Voyles 2013),

FIG. 5. Photographs of cloud and storm features from 2112 UTC 14 May (when the storm was a multicell complex) to 0037 15 May 2018 (when the storm was a supercell). Arrows at selected times point to the clear slot. RaXPol is also seen probing the storm at 2320 UTC. The tornado condensation funnel cloud is seen from 2336 to 2339 UTC. Since a variety of lenses of different focal lengths were used, the relative sizes of features varies. At 2112 UTC the view is to the west-southwest. The view from 2234 to 2320 UTC is to the northwest through north. The view from 2323 to 2336 UTC is to the northeast. The view from 2337 to 0037 UTC is to the east-northeast or east. Courtesy of H. Bluestein. Locations at the times given are found in Fig. 6.

increased in speed from 12.5 m s^{-1} at 2300 UTC to 20 m s^{-1} at 0100 UTC (Fig. 9b). Thus, the trend in the RAP data was supported by actual observations, though not in the near-storm environment. Such behavior is consistent with the diurnal variation in the boundary layer wind in the Southern Plains (e.g., Bluestein et al. 2018a), yet supercells do not typically turn suddenly when the NLLJ intensifies.

e. Visual appearance

We now correlate the visual appearance of the convective storm that developed into a supercell (Fig. 5) with its radar-observed characteristics from KICT (Figs. 7a,b). During the ordinary-cell/multicell phase the cloud base underneath the main updraft was located to the west/southwest of the precipitation, which was carried to the east-northeast by the winds aloft. At 2301 UTC, however, when the radar echo consolidated and propagated away from I-35, a lowered cloud base and short tail cloud appeared, along with a wall cloud (2308 UTC), visible as scud-like clouds extending downward from the northeasternmost lowered cloud base. During this time period RaXPol was deployed on the west side of Geuda Springs, Kansas.

FIG. 5. (*Continued*)

A time lapse video (supplemental material) indicated cyclonic rotation at cloud base. A clear slot, indicative of dry, sinking air, and sometimes preceding tornadoes (Lemon and Doswell 1979), appeared and broadened considerably over the next 11 min (2320 UTC). A funnel cloud first appeared from cloud base near the leading edge of the clear slot at 2323 UTC. It looked like a truncated cone, as it was flat at its bottom, rather than narrowing to a point. At about this time (2331 UTC) RaXPol was repositioned slightly to the east to follow the developing tornado. The tornado formed while the supercell began to eject the left-moving split member; this behavior is unusual because in many idealized simulations (and in

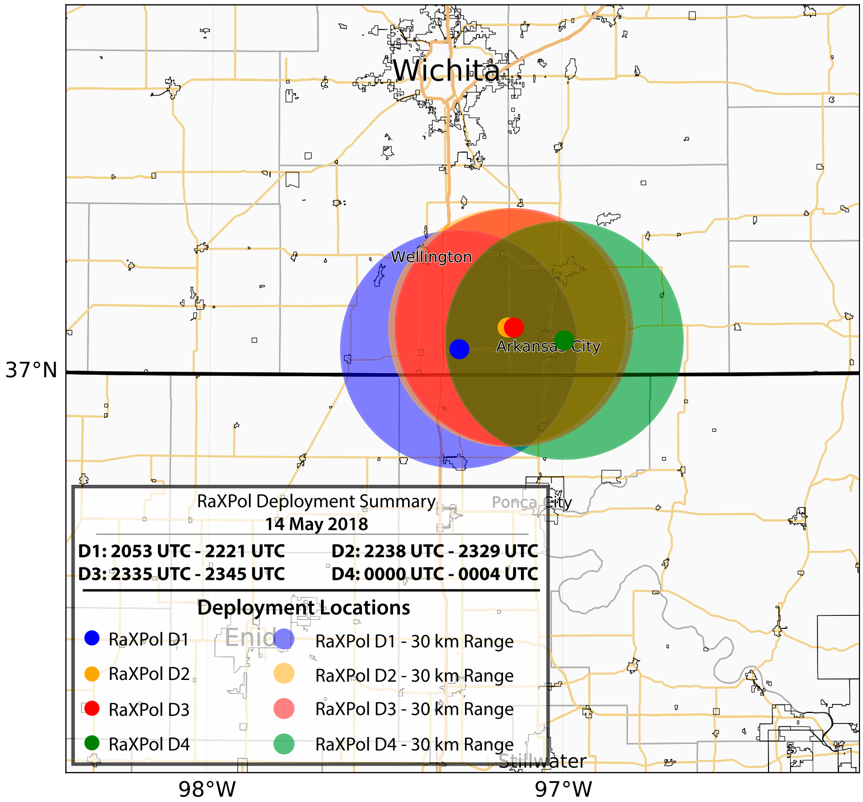

FIG. 6. Summary of RaXPol deployments (D1–D4) locations, times of data collection, and areas covered. Geuda Springs, KS, is located at D2.

observations), early on in the life of a convective storm, it splits and *subsequently* the right mover intensifies (e.g., Bluestein and Sohl 1979; Weisman and Klemp 1984). The funnel cloud subsequently developed into a more conventional-looking shape, coming to point at its bottom (2336 UTC), but did not extend all the way to the ground. It may have done so, but owing to intervening precipitation and dust, it was not visible from the vantage point of RaXPol. By 2337 the funnel cloud elongated, tilted, and contained a part of which was horizontal, as is sometimes seen when a tornado dissipates (e.g., Bluestein et al. 1988). The funnel cloud broke up into narrow, ropelike segments at 2339 UTC and disappeared shortly thereafter. The tornado was in progress from 2335 to 2340 UTC based on SPC storm data. An hour later, from another deployment location, the clear slot was vividly illuminated against darkened cloud bases associated with the RFGF (0037 UTC).

f. Storm evolution on the finescale

The evolution of the storm from the view of high-spatial-resolution radar data, from RaXPol, beginning ~2100 UTC, is depicted in Fig. 10. The finescale structure of two multicell complexes consisted of an earlier, more mature, broken line of cells (α), and a newer set of cells (β); the older cells within each complex were at the eastern ends, while the newest cells formed at the western edge. Much of the cores of the eastern cells did not appear to be associated with any active updrafts, just anvil debris with precipitation falling out; the western cores were associated with active, cumuliform cloud towers (Fig. 5; 2212 and 2234 UTC). By 2200 UTC the β complex consolidated into one mass, with an ‘‘Owl-Horn’’ echo at the rear edge (Kramar et al. 2005). Owl-Horn echoes have been found to be characteristic of some developing supercells and may be regarded as a sign of imminent storm evolution into a supercell. At 2238 UTC new discrete cells or pulses of convection continued to form at the rear of the main storm β. However, by 2300 UTC the β storm continued to become more isolated, with less, if any, new, discrete backbuilding on the rear flank of the storm. By 2325 UTC, as the tornado was forming, the echo looked like a classic supercell with a hook.

4. The relationship between satellite and radar-observed features

a. Locating the storm updraft

To determine the relationship between satellite-observed cloud-top observations and features hidden below, inside the storm, we considered evidence, but not direct measurement, of the main updraft via radar signatures, and the cloud-top infrared temperatures. Since multiple Doppler analyses of the wind field allowing for the kinematic estimate of vertical velocity were not possible, we considered two radar signatures commonly associated with updrafts: the Z_{DR} column and Z_{DR} rings or half rings (Ryzhkov et al. 1994; Kumjian and Ryzhkov 2008; Snyder et al. 2013; Kumjian et al. 2014) and the bounded weak-echo region (BWER) (e.g., Chisholm 1973; Lemon et al. 1978).

Z_{DR} columns and rings in numerical simulations are evidence of supercooled water drops (which are relatively flattened) lofted well above (1–3 km or more) the 0°C level in the environment and wet hail/graupel, and which produce relatively high values of Z_{DR} (in this case >3–4 dB). Snyder et al. (2017) found in highly idealized numerical simulations that rings tend to extend above Z_{DR} columns and that the best defined (widest and deepest/tallest) rings were those in simulations in which the environmental vertical shear is strong. Incomplete (e.g., half) rings were found near the center and forward (with respect to storm motion) of the updraft. To locate Z_{DR} columns/rings, polarimetric radar data need to be collected above the 0°C level in the environment, which is not always possible, especially when the radar is very close to the storm and is concentrating on probing tornadoes, which are at lower altitudes. Kumjian et al. (2010) suggested that the ring shape may be a result of graupel [and hail (Snyder et al. 2017)] falling along the right side (with respect to storm motion) of the updraft and experiencing wet growth in the presence of high liquid water content in the updraft. Below the 0°C level, the ring and half-ring shapes may be due to melting graupel and hail. Kumjian and Ryzhkov (2008) suggested that wet ice particles, which have high Z_{DR}, are advected in a curved trajectory around the mesocyclone aloft, resulting in the curved shape.

BWERs are evidence that in strong updrafts, the growth of more reflective precipitation particles is delayed until particles reach upper levels, while it is not delayed as much to higher altitudes on or outside the periphery of strong updrafts. In addition, hydrometeors in the updraft are evacuated from it. Data from KICT were used to locate Z_{DR} signatures at relatively high altitude and BWERs at middle levels, while RaXPol data were used to locate features with the highest possible spatial resolution at low altitude. Data from RaXPol were not available at higher elevation angles because scans were limited to angles less than ~10°–20° in an attempt to minimize the update time between volume scans while concentrating on the lowest levels, where tornadoes are most intense. A typical Z_{DR} half ring for this case study is shown at 2331 UTC (when the tornado was just appearing) at approximately 65 km southeast of KICT (Fig. 11a). At this range and an elevation angle of 4°, where it was best defined, the height of the half ring is ~4.75 km AGL, which, based on soundings at 0000 UTC (Fig. 4) was above, but not well above, the 0°C environmental temperature at 600 hPa, or ~4.3 km AGL. The corresponding BWER (Fig. 11b) is approximately collocated with the Z_{DR} half ring at 4° elevation; at 5.1° and 6.4° elevation the BWER is not apparent (Figs. 11c,d).

An idealized schematic of the relationship between Z_{DR} columns, rings, the weak-echo region (WER) and the radar echo of the storm is shown in Fig. 12a from Kumjian et al. (2014). In Fig. 12b, from Wienhoff et al. (2018), the close relationship between the Z_{DR} column and the updraft in a tornadic supercell, when dual-Doppler analyses were available to compute vertical velocities, was further confirmed. Few dual-Doppler analyses have afforded such confirmation (e.g., Conway and Zrnić 1993), while many other studies have involved numerical simulations, which depend upon how microphysics is represented in the model (e.g., Kumjian et al. 2014; Snyder et al. 2017). The main finding is that Z_{DR} columns are indeed well correlated with strong updrafts, though not perfectly: they tend to be offset slightly (e.g., Kumjian and Ryzhkov 2008) as in Fig. 12b. Conway and Zrnić (1993) and Loney et al. (2002) also found that the updraft center and BWER in some hailstorms are also offset from the region of enhanced Z_{DR}.

b. Evolution of cloud top

Although objective techniques have been developed for locating overshooting tops (Bedka et al. 2012), in this study the highest cloud top of the supercell was located manually where the IR (10.4 μm) cloud-top temperature was the coldest and probably represented an overshooting top. The evolution of the satellite-observed cloud top temperatures is depicted from when the storm was a multicell complex through when it produced a tornado, in Fig. 13. Cloud-top temperatures of only ~ −50°C were observed during the early multicell phase, prior to 2130 UTC. Small areas of cooler IR temperatures (~ −60° to −65°C) were apparent between 2130 and 2230 UTC, after which the multicell complex developed into a supercell. Beginning at

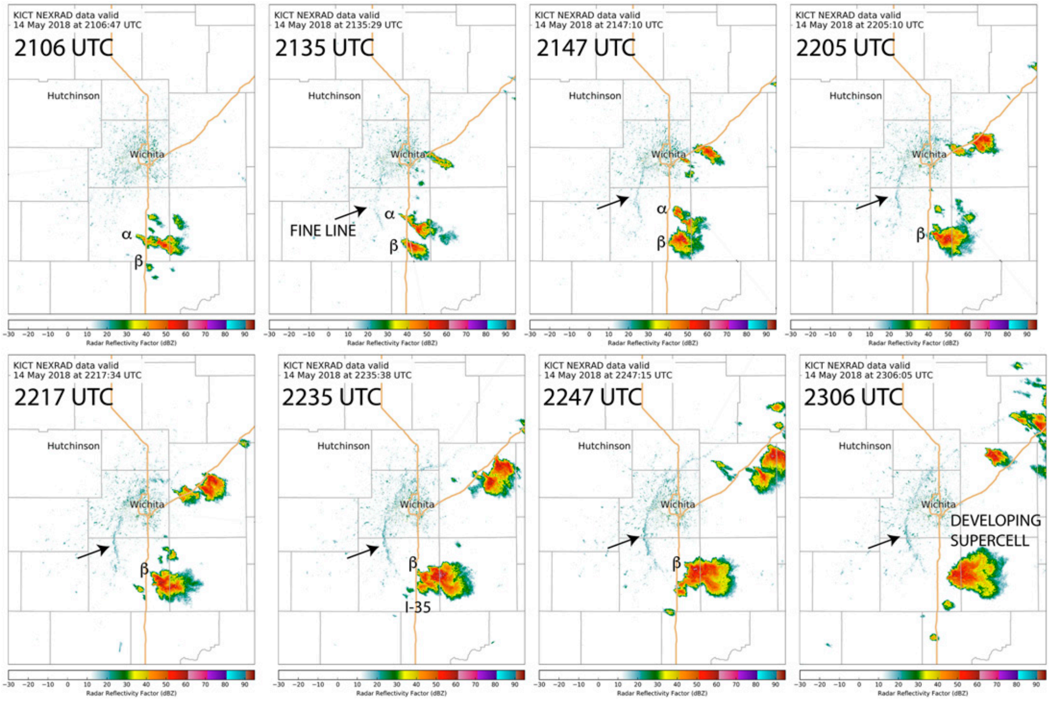

FIG. 7a. WSR-88D radar reflectivity on the mesoscale from KICT (Wichita, KS) color coded in dBZ from the early evolution of multicells (α and β) at 2106 UTC 14 May 2018, approximately every 10 min, until 2306 UTC, when multicell β was developing into a supercell. The arrow points to a fine line.

~2300 UTC, when the storm was becoming a supercell, a horseshoe-shaped or "enhanced-V" cold signature was visible (e.g., Negri 1982; McCann D. W. 1983; Heymsfield et al. 1983; Heymsfield and Blackmer 1988; Heymsfield et al. 1991; Homeyer 2014; Homeyer et al. 2017; Bedka et al. 2018), with coldest cloud tops ~ −74° to −76°C. Near and in the downstream direction (Fig. 13, 2330 and 2345 UTC) from the "enhanced V" there was a warm "hole" or "internal warm region" (Heymsfield et al. 1983). Beginning at 2330 UTC there were two separate warm regions, the southernmost one being associated with the right-moving, tornadic supercell, while the northernmost one was associated with the left mover. This might be the first observation of separate warm regions in the IR cloud top depiction of a splitting supercell and, as such, might suggest the possibility of using cloud-top IR temperatures from a satellite to observe/infer storm splitting.

The coldest temperatures might actually mark the tallest cloud tops, where the updrafts extend upward the highest and where the cloud material is advected around the overshooting top and downstream, while the relative maxima in temperatures represent depressions in the cloud top owing to subsidence and mixing of potentially warmer air from the stratosphere. It has also been postulated that the "enhanced-V" pattern might be due to the formation of a layer of cirrus clouds higher than the cumulonimbus anvil, in the stratosphere (e.g., Fujita 1982; Setvak et al. 2013). Differences in ice-water content could also affect the IR temperature field (Heymsfield et al. 1983; Heymsfield et al. 1991), for example, where there are fewer dense ice particles and the IR sensor on the satellite can penetrate down into the cloud farther, where the air is warmer. A summary of these mechanisms is illustrated in Fig. 14. Homeyer (2014), however, has argued that subsidence and variations in the ice water content in the anvil are not likely mechanisms and that cirrus in the stratosphere is the most likely explanation of the "enhanced-V" pattern. In summary, while there appears to be a relationship between the coldest IR top and the location of the overshooting top and main updraft in a supercell, their spatial correlation may not be exact.

The temporal evolution of the cloud top may be described in terms of the variation with time of the coldest IR cloud-top temperature (Fig. 15). From about 2152 to 2212 UTC, during the multicell phase of the storm, the IR cloud tops were quasi-steady, varying ~ ± 1°C from −61°C. From 2211 to 2221 UTC (~a 10-min period) there was a period of growth until the minimum cloud-top temperature plummeted to −73.5°C.

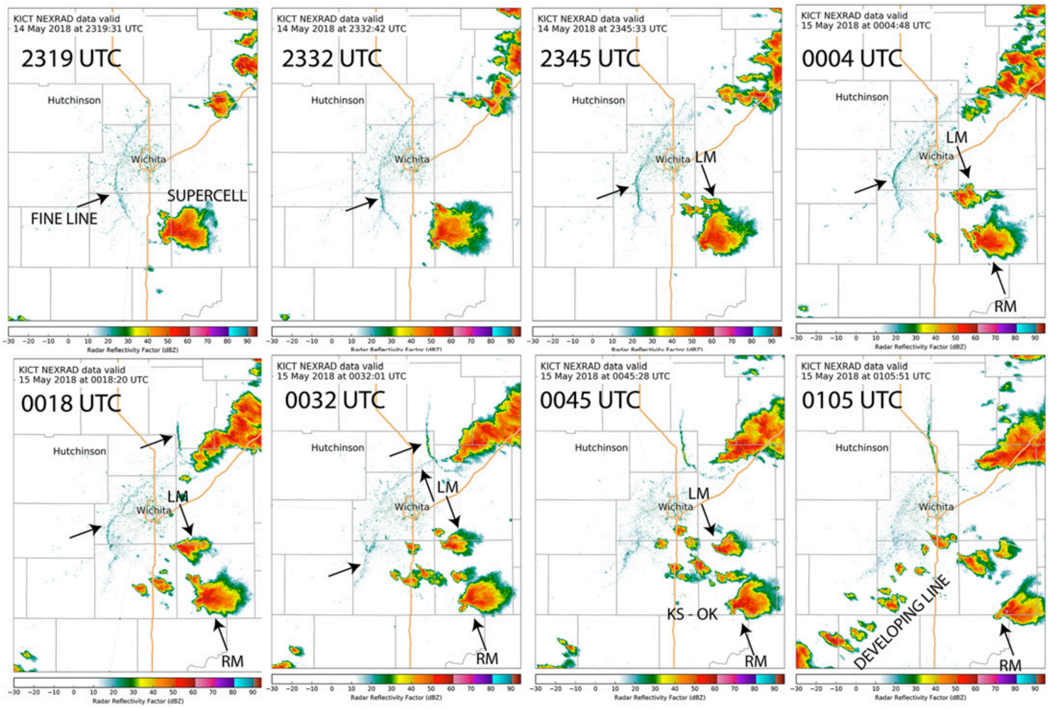

FIG. 7b. As in (a), but from 2319 UTC, before the supercell produced a tornado, through tornadogenesis, and tornado dissipation and beyond to 0105 UTC, when a line of new cells was forming southwest of Wichita. Splitting is indicated at 2345 UTC, shortly after the tornado had dissipated, as left-moving (LM) and right-moving (RM) cells. The LM appears to have formed on the north side of the supercell.

This minimum was followed by a several-minute collapse, as evidenced by an increase in IR cloud-top brightness temperature to ~ −65°C, after which there was another quasi-steady period until 2240 UTC. The increase in IR cloud-top temperature might not have represented an actual collapse, but instead, the appearance of above-anvil cirrus following the intensification of the updraft. This quasi-steady period was followed again by another 10-min growth period, during which the cloud top temperature dropped to −76.5°C, its lowest value in the period from ~2150 to 2340 UTC. This period of growth coincided approximately with the evolution of the multicells into a conglomerate cell, soon to become a supercell. For the next 10 min, the period of growth was reversed, as the cloud top collapsed, with its temperature increasing up to −68.5°. While the storm evolved into a supercell, there was sporadic growth for the next 10 min, not a period of quasi-steady behavior as in the previous two cycles. After ~2312 UTC, the IR cloud-top brightness temperature exhibited quasi-steady behavior, with the brightness temperature varying from ~ −73.5° to −70°C. After ~2341 UTC, when the tornado had dissipated, the top collapsed dramatically from −73.5°C to its early multicell phase level of ~ −60°C. The IR cloud-top brightness temperature was not documented after the tornado had dissipated. During the short time period when the tornado appeared, there was no apparent correlation with cloud-top brightness temperature, which was in a quasi-steady phase. It therefore appears as if there was a growth and collapse period totaling ~30 min just prior to the evolution of the multicell complex into a supercell, after which there was a quasi-steady period for ~30 min, during which tornadogenesis occurred; there was no strong indication of tornadogenesis, however, in the cloud-top brightness temperature tendency. Following tornadogenesis, there was a collapse of the cloud top. It is thus seen that tornadogenesis could not be inferred from cloud-top height, while supercell formation occurred during the growth and collapse of towers, and subsequent overall colder cloud-top brightness temperatures (higher cloud tops) than those documented during earlier multicell stages.

c. *Relationship among updrafts, cloud tops, and storm-scale features*

How various internal storm features were related to the location of the satellite-determined cloud-top locations is illustrated for selected times in Fig. 16, covering the late multicell phase, the development of the supercell, and the evolution of the supercell through

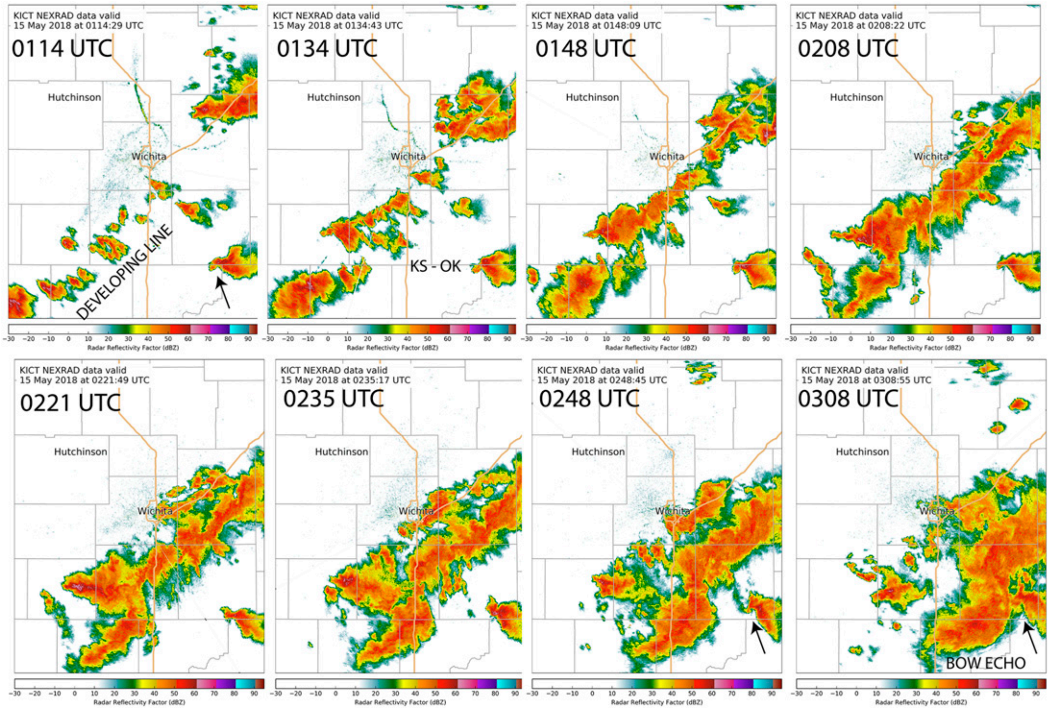

FIG. 7c. As in (a), but from 0114 UTC, when the supercell had slowed down its southeastward movement near the Kansas–Oklahoma border, until 0308 UTC, when the supercell was about to collide with an approaching bow echo.

tornadogenesis and the dissipation of the tornado.[1] Two different satellite overshooting-top locations were plotted: one based on the minimum IR brightness temperature and the other based on a more qualitative determination using the visible imagery. Visible overshooting tops can be found based on the shadows they cast on the surrounding clouds and the horizontal extent of the tops often consists of many pixels. There is therefore some uncertainty in the locations, particularly with the visible. This is illustrated in Fig. 17a, which is a zoomed-in version of the 0000 UTC panel of Fig. 3. The yellow "×" denotes the best guess at the highest location of the OT, but by that time a robust Above Anvil Cirrus Plume (AACP; Bedka et al. 2018) had formed, essentially shielding what was happening underneath. An orange "×" was placed at a location that may have an even higher OT. Note that these OT locations from the visible were made while looking at a series of subsequent 1-min images, as opposed to single images. The distance between these two possible OT locations was 6.9 km, providing an instantaneous estimate of the uncertainty in the visible location determination. At other times when an AACP is not present and the horizontal scale of the OT is less, the uncertainty is smaller. In the case of IR, we selected the pixel with the minimum IR brightness temperature that occurs coincident or very near the OT region found by brightness temperatures decreasing with time. Uncertainties from this method may result from 1) relatively large IR pixel sizes, 2) IR overshoots attaining a warmer temperature in the lower stratosphere, and 3) a residual AACP having a colder brightness temperature than a newer nearby OT. But in general, the IR uncertainties are less than that from the visible imagery. Figure 17b shows a visible/IR "sandwich" image (at the same time as Fig. 17a) which is created by making the IR image 70% transparent before overlaying it on the visible image. This allows us to see both the texture and shadows from the visible image along with the color-coded brightness temperatures in the IR. The white "×" is the location of one of the two coldest IR pixels, while the blue "×" is showing where the best estimate of the visible OT is located (same location as the yellow "×" in Fig. 17a). In both panels of Fig. 17, the AACP pointed to with arrows. Bedka et al. (2018) found that storms exhibiting an AACP are more likely to produce severe weather.

---

[1] The satellite-observed locations and the radar-observed locations were determined by two different coauthors, each working independently and, in order to be as objective as possible, no effort was made to try to fine tune the estimates of the locations.

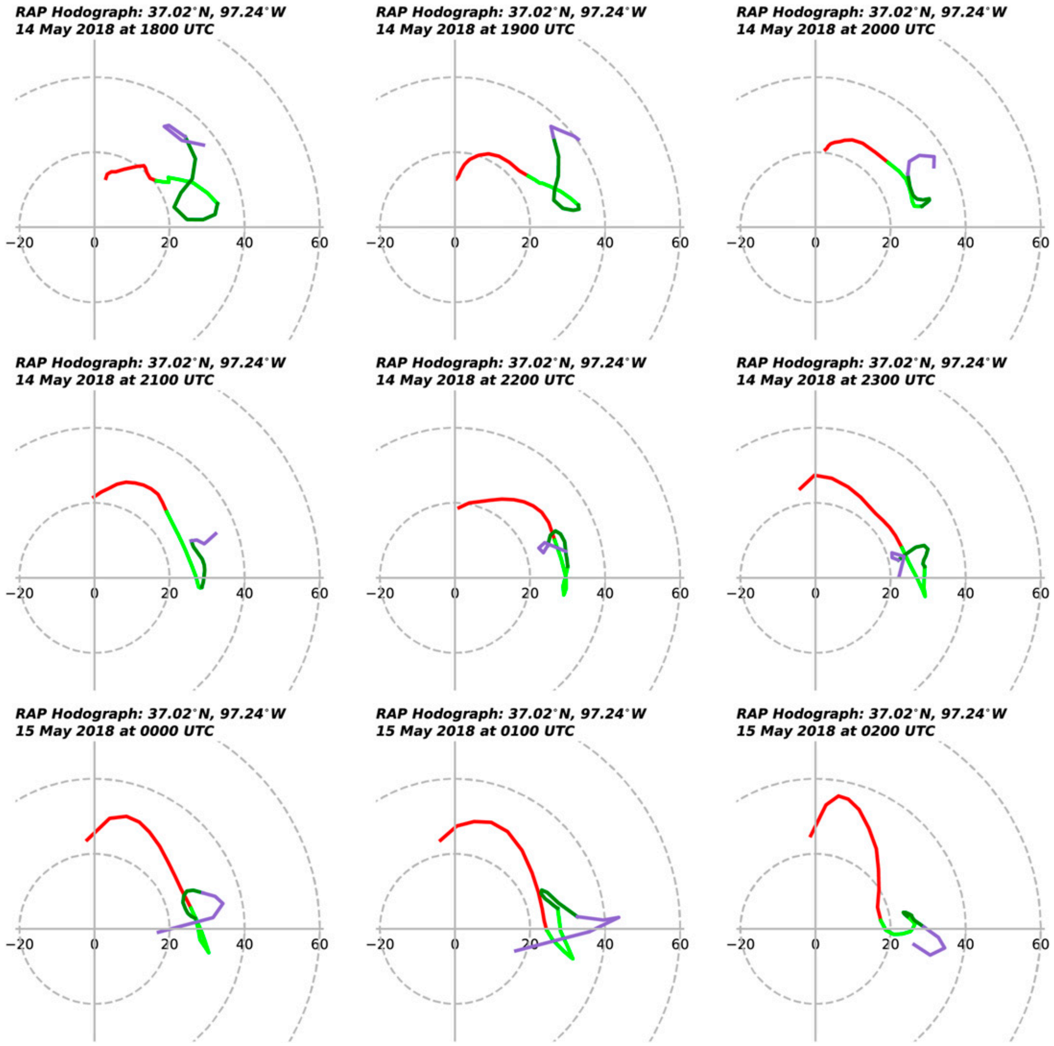

RAP Hodograph: 37.02°N, 97.24°W 14 May 2018 at 1800 UTC

RAP Hodograph: 37.02°N, 97.24°W 14 May 2018 at 1900 UTC

RAP Hodograph: 37.02°N, 97.24°W 14 May 2018 at 2000 UTC

RAP Hodograph: 37.02°N, 97.24°W 14 May 2018 at 2100 UTC

RAP Hodograph: 37.02°N, 97.24°W 14 May 2018 at 2200 UTC

RAP Hodograph: 37.02°N, 97.24°W 14 May 2018 at 2300 UTC

RAP Hodograph: 37.02°N, 97.24°W 15 May 2018 at 0000 UTC

RAP Hodograph: 37.02°N, 97.24°W 15 May 2018 at 0100 UTC

RAP Hodograph: 37.02°N, 97.24°W 15 May 2018 at 0200 UTC

FIG. 8. Hodographs (from RAP) near the location of the developing multicells, evolution into a tornadic supercell, and when the supercell stopped and changed direction, on 14–15 May 2018, at the times shown in UTC. Wind speeds shown in $\mathrm{m\,s^{-1}}$. Red, light green, dark green, and purple portions of the hodograph are for surface–700, 700–500, 500–300, and 300–200 hPa, respectively. The red and light green portions of the hodographs show the hodographs from the surface to ~3 km, and from ~3 to 6 km.

For these reasons we have plotted both the IR and visible locations in Fig. 16. For both the IR and visible overshooting tops, the cloud top locations were corrected for parallax at each time, based on the altitude of the radar echo tops. From KICT data at 2333 UTC (Figs. 11e,f), during the tornado, radar-echo top (actual cloud top could have been higher) was estimated to be ~17 km, assuming ''standard'' refraction conditions (4/3 Earth radius model) (Rinehart 1991; their Fig. 3.2). The actual cloud top observed from satellite will be at some altitude above the radar echo top, so we estimated 500 m above the radar echo top location when determining the amount of parallax correction to use. At the latitude and longitude of the storm, a 1- km error in the estimate of cloud-top height is associated with a 1.1 km shift in horizontal location due to parallax. The radii of the IR and visible circles in Fig. 16 indicate the range of uncertainty explained above. For example, the center of the solid circle at 0000 UTC in Fig. 16 has a parallax-corrected center near the yellow ''×'' in Fig. 17a and the orange ''×'' from Fig. 17a lies on the outer edge of the 6.9 km radius circle.

It is noted that the location of the updraft, as determined from the BWER and Z_{DR} locations, was not collocated with the radar-echo top, but rather was separated by ~10 km upstream. It is estimated that the locations of the updrafts and cloud tops, and the BWERs and Z_{DR} were known to within a circle of radius of 2 km,

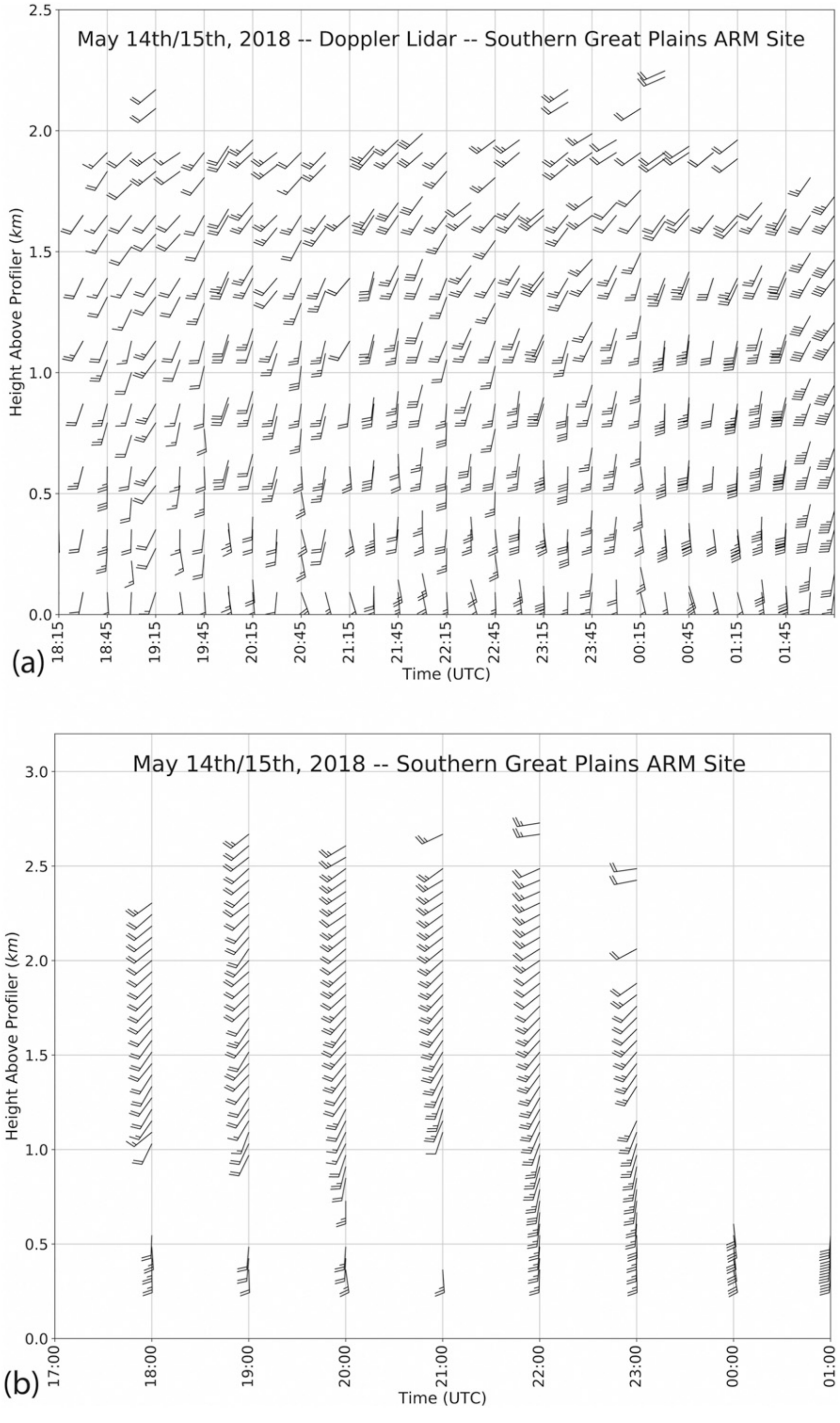

FIG. 9. Variation of winds with height above the instrument (km) as a function of time (UTC) on 14–15 May 2018. Half (whole) barbs denote 2.5 (5) m s^{-1}. At the Southern Great Plains ARM site in Lamont, OK, from (a) a Doppler lidar and (b) a 915 MHz Doppler wind profiler.

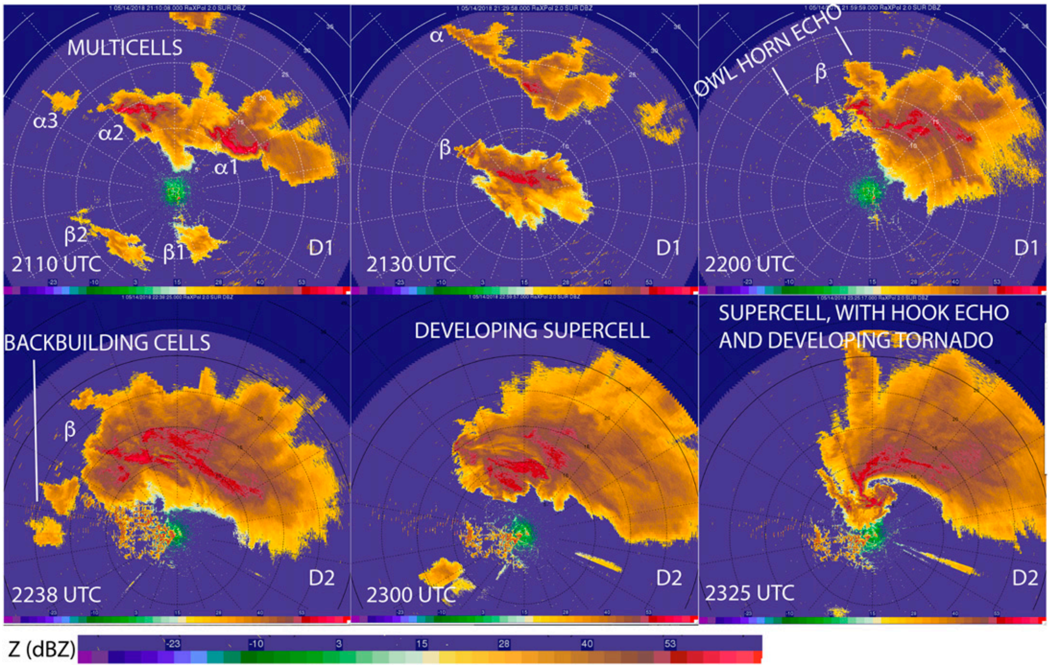

FIG. 10. Evolution of the multicell β into a supercell about to produce a tornado on 14 May 2018, as depicted by radar reflectivity images (dBZ) from RaXPol, on the fine scale. Range rings plotted every 5 km, at 2° elevation angle, from 2110 to 2325 UTC.

as indicated in Fig. 16. Uncertainties in the location of the updrafts are a result of the subjective and sometimes slightly ambiguous determination of the locations of the Z_{DR} and BWER locations, their representativeness of the location of the updrafts, any tilt in the updrafts, and in differences in the time between the available radar data and the available satellite imagery. Differences in time are greatest overall for KICT data, which were updated only every $\sim$4 min; RaXPol data, as noted earlier, were updated every 30 s or less. Assuming that the difference in time in between observing systems was at most 2 min, then the errors in locations of the radar-observed features were at most $\sim$800 m (given a storm motion of 6.6 m s^{-1}, determined subjectively by tracking the radar echo of the storm when it was a supercell, between 2300 and 0000 UTC), which is within the 2 km uncertainty assumed.

At 2221 UTC, during the multicell phase, there were several precipitation cores in storm β, but no Z_{DR} columns/rings or BWERs. The overshooting cloud top as located by satellite was along the southeastern edge of the most mature/easternmost cell. As the storm began to evolve into a supercell at 2253 UTC, the cells were consolidating and a Z_{DR} column/half-ring appeared near the junction of two echo cores, while there was no BWER and the overshooting top was located to the east of the Z_{DR} column/half ring in the most mature cell. At this time and all subsequent times, the uncertainty in the location of the visible OT was quite large (as shown by the large solid circles in Fig. 16), suggesting that we should focus on the IR OT location for comparisons with radar. While the supercell was maturing at 2311 UTC, the Z_{DR} column/half ring and a BWER aloft were located near a small spiral band in an evolving hook echo, while the overshooting top was located to the northeast. By 2321 UTC, when a tornado was soon to develop in the supercell, the overshooting top was still close to the updraft, but now in a more northward direction from the updraft, which was now located southeast of the hook echo, near the edge of the forward flank of the storm, near the weak-echo notch. In this case, the Z_{DR} half ring was located just to the west of the BWER; in Loney et al. (2002) this was also the case for a Z_{DR} column, while in Conway and Zrnić (1993) the Z_{DR} column was located just to the northwest of the BWER.

At 2336 UTC, when the tornado was beginning, the overshooting top was located very near the BWER along the tip of the hook, while the Z_{DR} half-ring was to their northwest. At this time a WEH and cyclonic vortex signature marked the location of the tornado. Although the bottom of the tornado funnel was not visible to us from our vantage point, there was a debris signature ($\rho_{\mathrm{hv}} < 0.8$) (Ryzhkov et al. 2005b;

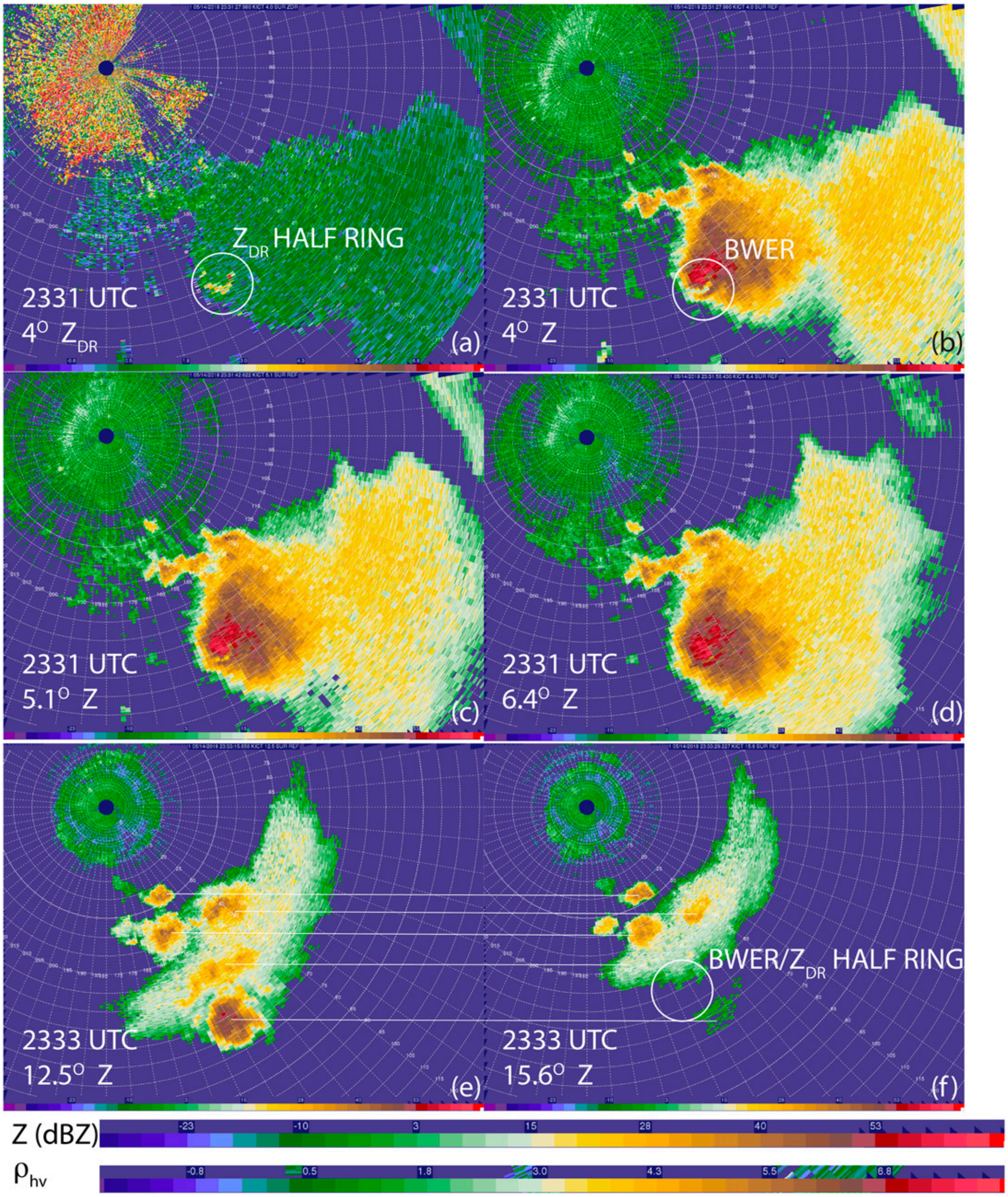

FIG. 11. Example of a Z_{DR} half ring and corresponding BWER at 2331 UTC 14 May 2018 when the tornado was beginning. (a) differential reflectivity at 4° elevation angle in dB; (b) as in (a), but for radar reflectivity in dBZ. From KICT, the WSR-88D radar at Wichita, KS. (c) As in (b), at 5.1° elevation angle; (d) as in (b), but at 6.4° elevation angle. Estimating the top of the radar echo in the supercell at 2333 UTC: (e),(f), as in (b), but at 12.5° and 15.6° elevation angles, respectively. Pairs of corresponding echoes at 12.5° and 15.6° elevation angles are joined by horizontal lines. The approximate BWER and Z_{DR} locations are indicated in (e) by a circle. Range rings are plotted every 5 km in all panels. The highest echo tops are not collocated with the locations of the updrafts at midlevels as inferred from the BWER and Z_{DR} half-ring locations.

Kumjian and Ryzhkov 2008) collocated with the vortex signature and WEH, supporting our claim that although we could not see a connection of the funnel cloud with the ground, there was in fact a tornado. Values of a copolar cross-correlation coefficient this low have been associated with debris in other tornadoes using X-band radars (e.g., Bluestein et al. 2007; Tanamachi et al. 2012; Houser et al. 2015, 2016; Bluestein et al. 2015, 2018b). An indication of the RFGF is given by the shift in Doppler velocity from away (yellow) to

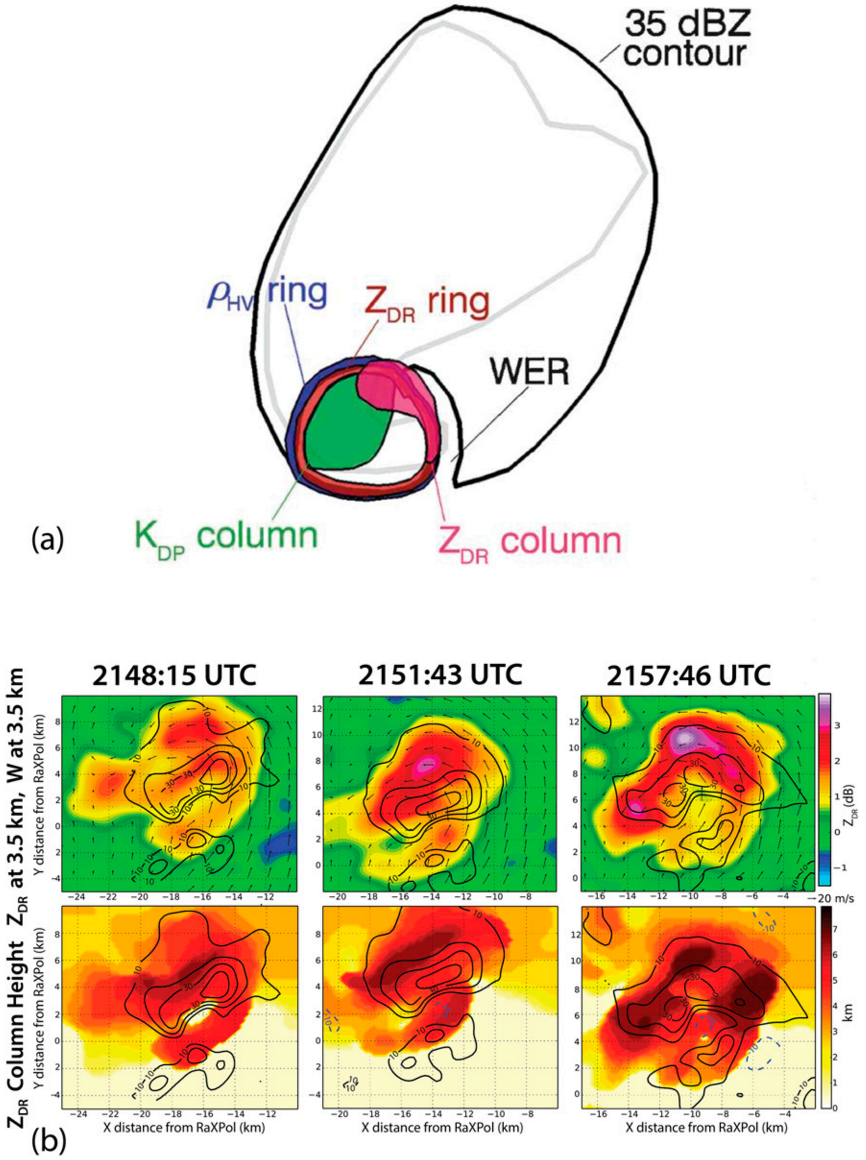

FIG. 12. Relative locations of Z_{DR} column, WER, and updrafts in a supercell from (a) an idealized schematic (Kumjian and Ryzhkov 2008) and (b) dual-Doppler analysis (Wienhoff et al. 2018). In (a), polarimetric features at midlevels (~5 km) are shown, along with outline of low-level 35 dBZ contour (thick black line). In (b) the horizontal wind field is plotted in the upper panels based on data from RaXPol and the WSR-88D at Twin Lakes (KTLX) for a tornadic supercell on 19 May 2013 between Edmond and Carney, OK, along with differential reflectivity Z_{DR} (dB) color coded and vertical velocity (contours labeled in m s^{-1}, every 10 m s^{-1}) at 3.5 km AGL; in the lower row of panels the Z_{DR} column height (the top of the column is at the altitude where Z_{DR} drops below 1 dB) is color coded in km and the vertical velocity is shown as in the top row of panels. The time of each panel is indicated in UTC.

toward (green) the radar, noted by the curved, white, dotted line in Fig. 16f at 2336 UTC. The BWER, which is located just ahead (to the southeast) of the RFGF, is consistent with the notion of occluding cyclic mesocyclogenesis, during which a new updraft and mesocyclone form along the leading edge of a kink in the RFGF, leaving an older occluded mesocyclone behind (e.g., Adlerman et al. 1999; Adlerman and Droegemeier 2005); at 2311 UTC, the BWER and Z_{DR} columns were located near the front edge of the developing hook, while at 2336 UTC they had migrated back into the mainly body of the storm, and a new

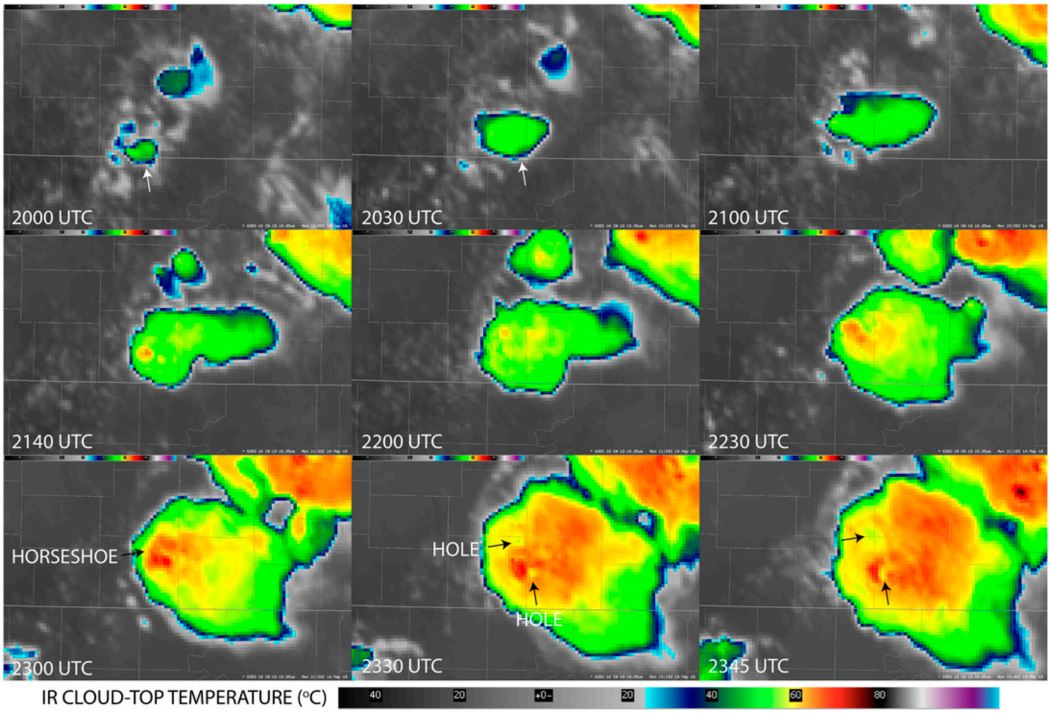

FIG. 13. *GOES-16* 10.4 μm infrared brightness temperature (°C) from the *GOES-16* satellite as function of time (UTC) on 14 May 2018, covering the period from storm initiation until the tornado had just dissipated in the supercell. The horseshoe cold pattern ("enhanced-V") signature and warm holes ("internal warm regions") are pointed out during the supercell phase of the storm.

BWER suggestive of a new updraft jumped ahead. After the tornado had dissipated, at 2344 UTC the Z_{DR} half ring, BWER, and overshooting top *all* had jumped to a location ahead (southeast) of the hook echo, again, consistent with the conceptual model for cyclic mesocyclogenesis. The Z_{DR} half ring was located just to the west-southwest of the BWER, not exactly to the west, as it was earlier. At 0002 UTC, the overshooting top, BWER, and Z_{DR} were still in close proximity, but now the IR cloud top was located to the west of the BWER, which was in turn located just to the west of the Z_{DR} half ring. No further RaXPol data were collected after 0002 UTC, because after the radar truck had been farther repositioned to the southeast to keep up with the storm, the radar could no longer collect data owing to a hardware malfunction.

In Fig. 18 the relationships among the satellite-derived overshooting top (both visible and IR, as in Fig. 16), the Z_{DR} updraft column/half ring, and the BWER as a function of time are shown graphically. Between 2221 and 2253 UTC there is a jump in location of the overshooting top to the north/northeast, which is anomalous with respect to the subsequent behavior of the overshooting top locations, and probably a result of a new updraft appearing north/northeast of the older one (not shown; based on animations of IR imagery at 1-min intervals between ~2220 and ~2340 UTC), during the multicell phase of the storms; in these animations it is seen that a new brightness temperature minimum occurs to the north in a new overshooting top to the north of the previous one. Although both the absolute and relative locations of all the cloud tops, Z_{DR} updraft signatures, and BWERs must be treated with caution owing to uncertainties, it appears that prior to tornadogenesis and continuing up to tornadogenesis, during the supercell phase (from ~2253 to 2336), the locations of the overshooting top were in general located to the northeast of the updraft as inferred from the Z_{DR} and BWER location. The evidence presented in Fig. 16 pointed to the process of cyclic mesocyclogenesis as being possibly related to this shift in location. However, no tornadoes were reported with this new cycle; tornadoes were not observed until several hours later (~0300 UTC), after the supercell had changed direction and retreated back into Kansas from Oklahoma.

5. Summary and conclusions

This study was an effort to determine observationally the relationship between the main updraft

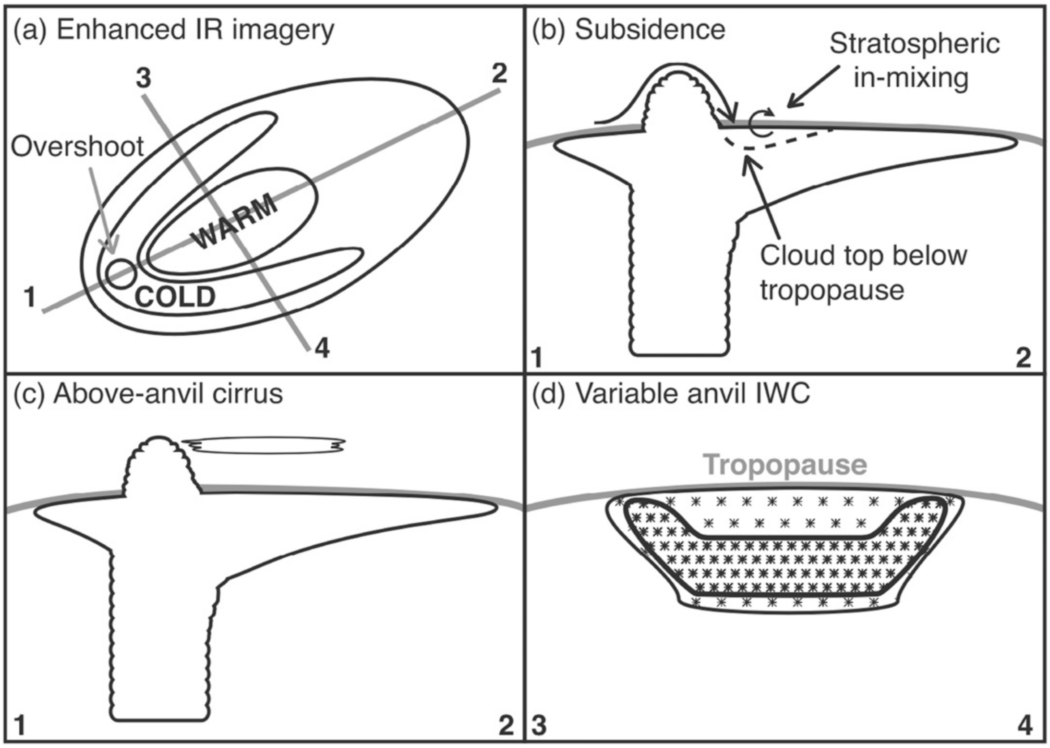

FIG. 14. Three possible mechanisms for the formation of the "enhanced-V" cold area and "internal warm region" (a) at the top of cumulonimbus clouds having overshooting tops. In (b) subsidence over the overshooting top accompanied by vertical mixing; in (c) above-anvil cirrus; and in (d) horizontal variations in anvil ice-water content (from Homeyer 2014).

in a tornado-producing supercell and the highest (overshooting) cloud top, using available radar and satellite data. It was found from a synthesis of the best-available ground-based, mobile, rapid scan polarimetric radar data and geosynchronous satellite visible and IR imagery that the storm top was related to the updraft below as follows: 1) The highest cloud top during the period spanning from when the storm was an intensifying multicell to when it became a supercell was near the highest echo top. 2) After tornadogenesis, however, the highest echo top was consistently about 10 km to the northeast of the updraft and highest cloud top. This displacement could have been the result of a tilted updraft in presence of propagation to the southeast and westerly overall deep shear; in the soundings shown in Fig. 4, the surface winds were from approximately the south, while above ~7.5 km AGL, the winds were mostly from the west or west southwest at ~20–25 m s^{-1}. The displacement could also have been caused by a delay in the precipitation reaching the top of the storm (and penetrating into the stratosphere) 3) Just after tornadogenesis, the updraft as located by the Z_{DR} ring appeared to be left behind to the north of the tornado, while the cloud top and BWER jumped ahead of the tornado and hook echo, probably owing to the cyclic mesocyclogenesis process, during which a new updraft formed along the bulge in the surface RFGF, while the previous updraft occluded. This conclusion is tentative, owing to the

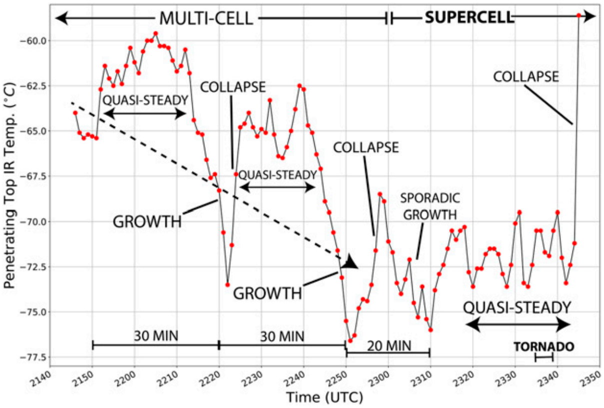

FIG. 15. The temporal (time in UTC on 14 May 2018) evolution of the IR cloud-top temperature from the *GOES-16* satellite, covering the multicell phase of the storm and the supercell phase just until the dissipation of the first tornado. Periods of cloud-top growth (rapid decreases in cloud-top IR temperature) and collapse (rapid increases in cloud-top temperature) are highlighted, along with periods of quasi-steady behavior.

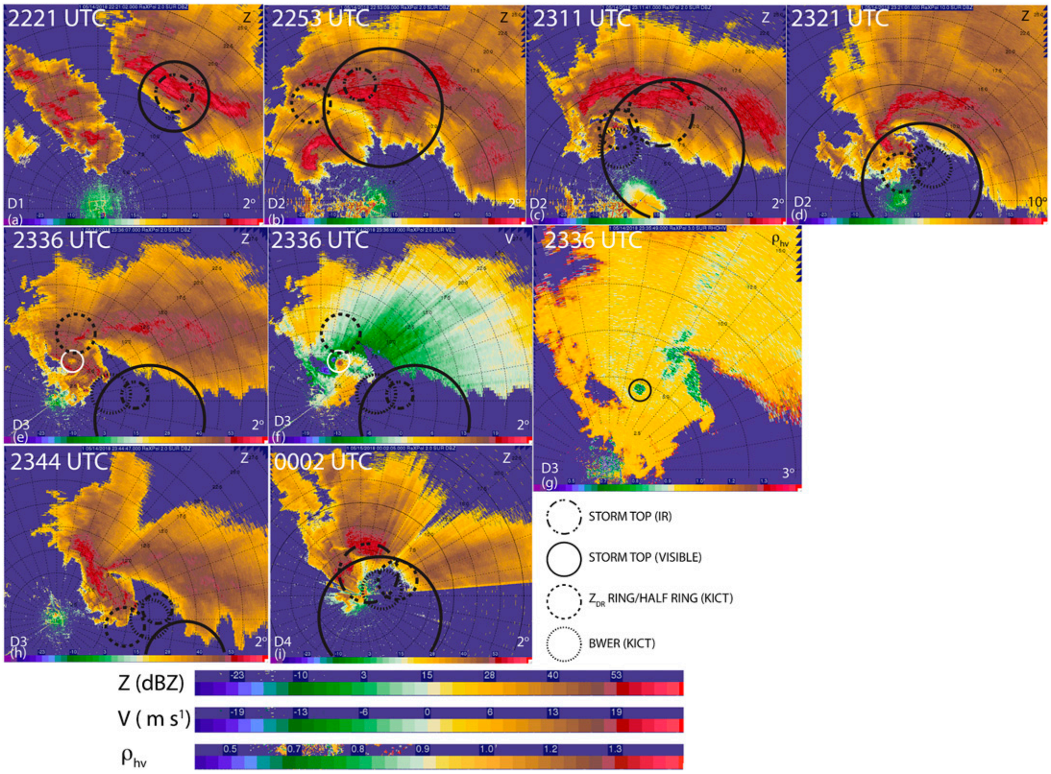

FIG. 16. (a),(b),(c),(d),(e),(f),(h),(i) Selected radar imagery from RaXPol on 14 May 2018, illustrating the relationship between the locations of the storm *GOES-16* IR cloud top (dash–dot circles), *GOES-16* VIS overshooting tops (solid circles), the Z_{DR} rings/half rings (dashed circles), and the BWERs (dotted circles) from KICT, at midlevel elevation angles. In all but (f),(g), the radar reflectivity is displayed (in dBZ, color coded). In (f) Doppler velocity (m s^{-1}) is color coded and in (g) ρ_{hv} is color coded. In (e)–(g), the locations of the tornado based on the WEH (white circle), cyclonic shear signature (white circle), and debris signature [black circle; relatively low (<0.8) ρ_{hv}] are shown, respectively. In (f) the approximate location of the RFGF (shift from receding, yellow Doppler velocities, to approaching, green, Doppler velocities) is denoted by a curved, white dotted line. The radius of all the circles indicates the uncertainties in locating the radar and satellite features; note the much greater uncertainty in the location of the visible cloud tops. The elevation angles and deployment designation are also shown in each panel. The sequence of radar imagery is shown at ~10–15 min intervals; time shown in UTC. Range rings are plotted every 2.5 km.

difficulty in locating the storm top by satellite at ~2344–2346 UTC. 4) No signature in the satellite data was apparent that could be correlated with tornadogenesis. In this case there did not appear to be an indication in the satellite imagery that could have been used to infer or predict tornadogenesis. 5) Separate overshooting tops were noted after the supercell had split. This may be the first time this has been observed by satellite[2] and holds open the possibility of using satellite imagery to track splitting storms. We can also conclude that despite the visible band being higher resolution, pinpointing OT locations with IR imagery using the coldest pixel has less uncertainty than using visible imagery.

While the results from this study add to our knowledge of how the internal parts of a tornadic supercell are related to features detectable at storm top, there are a number of shortcomings that need to be overcome: Although the mobile Doppler radar data were of high spatiotemporal resolution, they were not collected near or above the environmental 0°C level where Z_{DR} updraft signatures are found, in order to maintain as low a volumetric update time as possible necessary for high-quality tornadogenesis studies; we had to, in this case, use surveillance radar data from 65 km away to locate Z_{DR} updraft signatures, which resulted in coarser spatial resolution, and the volumetric update time of this radar was much less frequent than that of the mobile radar. There were no other nearby (within ~10–20 km) mobile Doppler

---

[2] Lindsey and Bunkers (2005) documented a splitting supercell over eastern Oklahoma using *GOES-12* imagery, but documentation of overshooting tops in both of the split cells was not described.

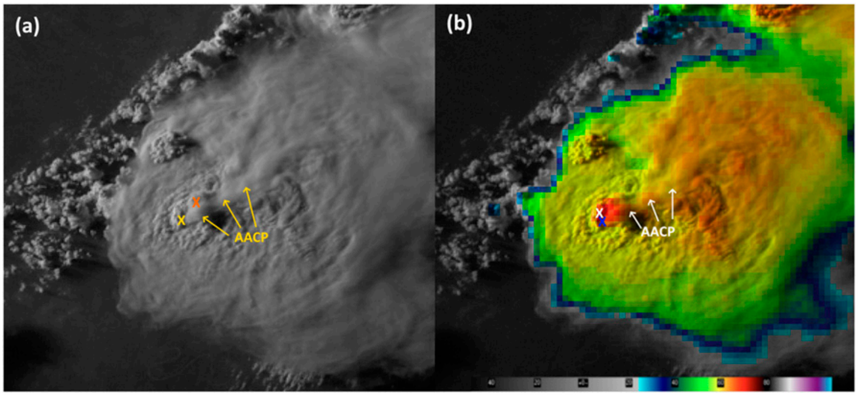

FIG. 17. (a) *GOES-16* band 2 visible satellite image from 0000 UTC 15 May 2018. The yellow "×" denotes the best guess at the highest portion of the overshooting top derived from a series of visible images, while the orange "×" shows the farthest away possible location. (b) *GOES-16* band2/band 13 visible/IR "sandwich" image from the same time. The blue "×" is in the same location as the yellow "×" in panel (a), and the white "×" is the location of one of the two coldest IR pixels. The IR legend is the same used in Fig. 13. The above anvil cirrus plume (AACP) is pointed out in both frames. Note that these denoted OT locations are not yet parallax-corrected so that they match up with the cloud-top features of interest.

radars or fixed-site radars collecting data, so vertical velocity could not be quantified by dual-Doppler analysis.

In the future, we could collect data up to and above the environmental 0°C level by sacrificing temporal resolution for spatial coverage. If, for example, RaXPol were to scan up to 40° elevation angle at a range of 10 km, coverage to 8 km AGL, which would be well above the environmental 0°C level, would be achieved. Scanning to this height would result in a volumetric update time, assuming scanning elevation increments of 2°, of ~45 s, which is still less than the 1-min of the satellite, though 30-s intervals are possible for the satellite. For relatively high elevations, however, it would be necessary to account for the polarimetric reflectivity measurements being made away from the true vertical and horizontal (Bringi and Chandrasekar 2001; Ryzhkov et al. 2005a). Having a companion rapid-scan Doppler radar would allow for the possibility of dual-Doppler analysis of the wind field (e.g., Bluestein et al. 1995; Wurman et al. 2007; Wurman et al. 2010), from which vertical velocity could be estimated.

In addition, an overflying aircraft having a downward looking radar such as the EDOP in the NASA ER-2 could be used to probe the top of the storm, as done by Heymsfield et al. (1996, 2013), though with much longer updates because it takes a number of minutes for the aircraft execute its flight pattern. Such information would be useful or even critical in locating updrafts near storm top and correlating overshooting top locations with updrafts in the storm interior below. Finally, a mobile, rapid scan (partially electronically scanning using imaging-radar techniques), C-band, polarimetric, Doppler radar is currently being developed and built at OU. This radar will have the capability of scanning the entire volume of a storm up to 45° elevation approximately every 6–10 s. It would therefore be well suited for rapid polarimetric observations to storm top, when it is expected to be available, in 2021 (Salazar et al. 2019). With these additional instruments, it should be possible to determine the internal structure of a

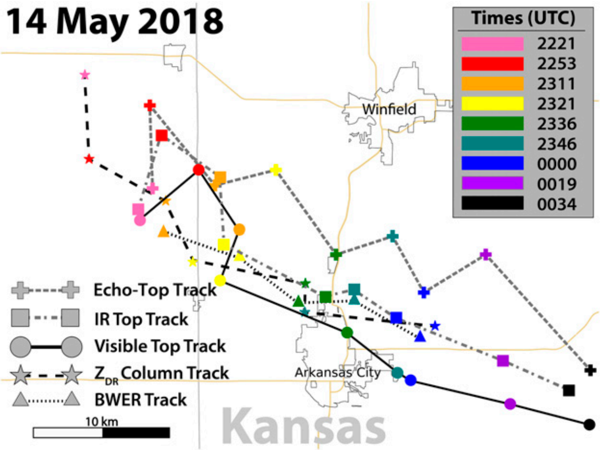

FIG. 18. The tracks of the overshooting tops from the visible *GOES-16* imagery (shaded circles), the overshooting tops from the coldest *GOES-16* IR pixel (shaded squares), Z_{DR} column/ring/half rings (shaded stars; based on KICT data), and BWER tracks (shaded triangle; based on KICT data), on 14 May 2018 at the color-coded times in UTC. The overshooting top track crosses over the Z_{DR} and BWER tracks when the tornado is in progress (~2336 UTC).

supercell and compare it to satellite cloud top information with unprecedented precision.

Acknowledgments. NSF Grant AGS-1560945 funded this study. RaXPol was built with support from MRI grant from NSF Grant AGS-0821231. The maintenance of RaXPol is supported by the Advanced Radar Research Center (ARRC) at the University of Oklahoma (OU). We are indebted to Boon-Leng Cheong, Danny Feland, Tian Yu, and Bob Palmer at the ARRC for their support of RaXPol. Cameron Homeyer (OU) provided GridRad data. The views, opinions, and findings in this report are those of the authors and should not be construed as an official NOAA and/or U.S. government position, policy, or decision.

REFERENCES

Adlerman, E. J., and K. K. Droegemeier, 2005: The dependence of numerically simulated cyclic mesocyclogenesis upon environmental vertical wind shear. *Mon. Wea. Rev.*, **133**, 3595–3623, https://doi.org/10.1175/MWR3039.1.

——, ——, and R. Davies-Jones, 1999: A numerical simulation of cyclic mesocyclogenesis. *J. Atmos. Sci.*, **56**, 2045–2069, https://doi.org/10.1175/1520-0469(1999)056<2045:ANSOCM>2.0.CO;2.

Bedka, K. M., R. Dworak, J. Brunner, and W. Feltz, 2012: Validation of satellite-based objective overshooting cloud-top detection methods using *CloudSat* cloud profiling radar observations. *J. Appl. Meteor. Climatol.*, **51**, 1811–1822, https://doi.org/10.1175/JAMC-D-11-0131.1.

Bedka, K., E. M. Murillo, C. R. Homeyer, B. Scarino, and H. Mersiovsky, 2018: The above-anvil cirrus plume: An important severe weather indicator in visible and infrared satellite imagery. *Wea. Forecasting*, **33**, 1159–1181, https://doi.org/10.1175/WAF-D-18-0040.1.

Benjamin, S. G., and Coauthors, 2016: A North American hourly assimilation and model forecast cycle: The Rapid Refresh. *Mon. Wea. Rev.*, **144**, 1669–1694, https://doi.org/10.1175/MWR-D-15-0242.1.

Bluestein, H. B., and C. J. Sohl, 1979: Some observations of a splitting severe thunderstorm. *Mon. Wea. Rev.*, **107**, 861–873, https://doi.org/10.1175/1520-0493(1979)107<0861:SOOASS>2.0.CO;2.

——, and M. H. Jain, 1985: Formation of mesoscale lines of precipitation: Severe squall lines in Oklahoma during the spring. *J. Atmos. Sci.*, **42**, 1711–1732, https://doi.org/10.1175/1520-0469(1985)042<1711:FOMLOP>2.0.CO;2.

——, E. W. McCaul Jr., G. P. Byrd, and G. R. Woodall, 1988: The unsual dissipation of a tornado funnel. *Mon. Wea. Rev.*, **116**, 950–952, https://doi.org/10.1175/1520-0493(1988)116<0950:TUDOAT>2.0.CO;2.

——, A. L. Pazmany, J. C. Galloway, and R. E. McIntosh, 1995: Studies of the substructure of severe convective storms using a mobile 3-mm-wavelength Doppler radar. *Bull. Amer. Meteor. Soc.*, **76**, 2155–2169, https://doi.org/10.1175/1520-0477(1995)076<2155:SOTSOS>2.0.CO;2.

——, C. C. Weiss, and A. L. Pazmany, 2003: Mobile Doppler radar observations of a tornado in a supercell near Bassett, Nebraska, on 5 June 1999. Part I: Tornadogenesis. *Mon. Wea. Rev.*, **131**, 2954–2967, https://doi.org/10.1175/1520-0493(2003)131<2954:MDROOA>2.0.CO;2.

——, M. M. French, R. L. Tanamachi, S. Frasier, K. Hardwick, F. Junyent, and A. L. Pazmany, 2007: Close-range observations of tornadoes in supercells made with a dual-polarization, X-band, mobile Doppler radar. *Mon. Wea. Rev.*, **135**, 1522–1543, https://doi.org/10.1175/MWR3349.1.

——, ——, I. PopStefanija, R. T. Bluth, and J. B. Knorr, 2010: A mobile, phased-array Doppler radar for the study of severe convective storms: The MWR-05XP. *Bull. Amer. Meteor. Soc.*, **91**, 579–600, https://doi.org/10.1175/2009BAMS2914.1.

——, J. C. Snyder, and J. B. Houser, 2015: A multiscale overview of the El Reno, Oklahoma, tornadic supercell of 31 May 2013. *Wea. Forecasting*, **30**, 525–552, https://doi.org/10.1175/WAF-D-14-00152.1.

——, M. M. French, J. C. Snyder, and J. B. Houser, 2016: Doppler radar observations of anticyclonic tornadoes in cyclonically rotating, right-moving supercells. *Mon. Wea. Rev.*, **144**, 1591–1616, https://doi.org/10.1175/MWR-D-15-0304.1.

——, G. S. Romine, R. Rotunno, D. W. Reif, and C. C. Weiss, 2018a: On the anomalous counterclockwise turning of the surface wind with time in the Plains of the United States. *Mon. Wea. Rev.*, **146**, 467–484, https://doi.org/10.1175/MWR-D-17-0297.1.

——, K. J. Thiem, J. C. Snyder, and J. B. Houser, 2018b: The multiple-vortex structure of the El Reno, Oklahoma, tornado on 31 May 2013. *Mon. Wea. Rev.*, **146**, 2483–2502, https://doi.org/10.1175/MWR-D-18-0073.1.

——, ——, ——, and ——, 2019: Tornadogenesis and early evolution in the El Reno, Oklahoma, supercell on 31 May 2013. *Mon. Wea. Rev.*, **147**, 2045–2066, https://doi.org/10.1175/MWR-D-18-0338.1.

Bringi, V. N., and V. Chandrasekar, 2001: *Polarimetric Doppler Weather Radar: Principles and Applications*. Cambridge University Press, 636 pp.

Brown, R. A., L. R. Lemon, and D. W. Burgess, 1978: Tornado detection by pulsed Doppler radar. *Mon. Wea. Rev.*, **106**, 29–38, https://doi.org/10.1175/1520-0493(1978)106<0029:TDBPDR>2.0.CO;2.

——, R. M. Steadham, B. A. Flickinger, R. R. Lee, D. Sirmans, and V. T. Wood, 2005: New WSR-88D volume coverage pattern 12: Results of field tests. *Wea. Forecasting*, **20**, 385–393, https://doi.org/10.1175/WAF848.1.

Byko, Z., P. M. Markowski, Y. Richardson, J. Wurman, and E. Adlerman, 2009: Descending reflectivity cores in supercell thunderstorms observed by mobile radars and in a high-resolution numerical simulation. *Wea. Forecasting*, **24**, 155–186, https://doi.org/10.1175/2008WAF2222116.1.

Chisholm, A. J., 1973: Part I: Radar case studies and airflow models. *Alberta Hailstorms, Meteor. Monogr.*, No. 36, Amer. Meteor. Soc., 1–36.

Coffer, B. E., and M. D. Parker, 2015: Impacts of increasing low-level shear on supercells during the early evening transition. *Mon. Wea. Rev.*, **143**, 1945–1969, https://doi.org/10.1175/MWR-D-14-00328.1.

Conway, J. W., and D. S. Zrnić, 1993: A study of embryo production and hail growth using dual-Doppler and multiparameter radars. *Mon. Wea. Rev.*, **121**, 2511–2528, https://doi.org/10.1175/1520-0493(1993)121<2511:ASOEPA>2.0.CO;2.

Cooney, J. W., K. P. Bowman, C. R. Homeyer, and T. M. Fenske, 2018: Ten year analysis of tropopause-overshooting convection using GridRad data. *J. Geophys. Res. Atmos.*, **123**, 329–343, https://doi.org/10.1002/2017JD027718.

Crum, T. D., and R. L. Alberty, 1993: The WSR-88D and the WSR-88D Operational Support Facility. *Bull. Amer. Meteor. Soc.*, **74**, 1669–1687, https://doi.org/10.1175/1520-0477(1993)074<1669:TWATWO>2.0.CO;2.

——, ——, and D. W. Burgess, 1993: Recording, archiving, and using WSR-88D data. *Bull. Amer. Meteor. Soc.*, **74**, 645–653, https://doi.org/10.1175/1520-0477(1993)074<0645:RAAUWD>2.0.CO;2.

Davies-Jones, R. P., and H. Brooks, 1993: Mesocyclogenesis from a theoretical perspective. *The Tornado: Its Structure, Dynamics, Prediction, and Hazards, Geophys. Monogr.*, No. 79, Amer. Geophys. Union, 105–114.

Dowell, D. C., C. R. Alexander, J. M. Wurman, and L. J. Wicker, 2005: Centrifuging of hydrometeors and debris in tornadoes: Radar-reflectivity patterns and wind-measurement errors. *Mon. Wea. Rev.*, **133**, 1501–1524, https://doi.org/10.1175/MWR2934.1.

Dworak, R., K. Bedka, J. Brunner, and W. Feltz, 2012: Comparison between *GOES-12* overshooting-top detections, WSR-88D radar reflectivity, and severe storm reports. *Wea. Forecasting*, **27**, 684–699, https://doi.org/10.1175/WAF-D-11-00070.1.

Eskridge, R. E., and P. Das, 1976: Effect of a precipitation–driven downdraft on a rotating wind field: A possible trigger mechanism for tornadoes? *J. Atmos. Sci.*, **33**, 70–84, https://doi.org/10.1175/1520-0469(1976)033<0070:EOAPDD>2.0.CO;2.

French, M. M., H. B. Bluestein, I. PopStefanija, C. A. Baldi, and R. T. Bluth, 2013: Reexamining the vertical development of tornadic vortex signatures in supercells. *Mon. Wea. Rev.*, **141**, 4576–4601, https://doi.org/10.1175/MWR-D-12-00315.1.

Fujita, T. T., 1982: Principle of stereoscopic height computations and their applications to stratospheric cirrus over severe thunderstorms. *J. Meteor. Soc. Japan*, **60**, 355–368, https://doi.org/10.2151/jmsj1965.60.1_355.

——, G. S. Forbes, and T. A. Umenhofer, 1976: Close-up view of 20 March 1976 tornadoes: Sinking cloud tops to suction vortices. *Weatherwise*, **29**, 116–145, https://doi.org/10.1080/00431672.1976.10544142.

Gaudet, B. J., and W. R. Cotton, 2006: Low-level mesocyclonic concentration by nonaxisymmetric transport. Part I: Supercell and mesocyclone evolution. *J. Atmos. Sci.*, **63**, 1113–1133, https://doi.org/10.1175/JAS3685.1.

Heymsfield, G. M., and R. H. Blackmer Jr., 1988: Satellite-observed characteristics of Midwest severe thunderstorm anvils. *Mon. Wea. Rev.*, **116**, 2200–2224, https://doi.org/10.1175/1520-0493(1988)116<2200:SOCOMS>2.0.CO;2.

——, G. Szejwach, S. Schotz, and R. H. Blackmer Jr., 1983: Upper-level structure of Oklahoma tornadic storms on 2 May 1979. II: Proposed explanation of "V" pattern and internal warm region in infrared observations. *J. Atmos. Sci.*, **40**, 1756–1767, https://doi.org/10.1175/1520-0469(1983)040<1756:ULSOOT>2.0.CO;2.

——, R. Fulton, and J. D. Spinhirne, 1991: Aircraft overflight measurements of Midwest severe storms: Implications on geosynchronous satellite interpretations. *Mon. Wea. Rev.*, **119**, 436–456, https://doi.org/10.1175/1520-0493(1991)119<0436:AOMOMS>2.0.CO;2.

——, and Coauthors, 1996: The EDOP radar system on the high-altitude NASA ER-2 aircraft. *J. Atmos. Oceanic Technol.*, **13**, 795–809, https://doi.org/10.1175/1520-0426(1996)013<0795:TERSOT>2.0.CO;2.

——, L. Tian, L. Li, M. McLinden, and J. I. Cervantes, 2013: Airborne radar observations of severe hailstorms: Implications for future spaceborne radar. *J. Appl. Meteor. Climatol.*, **52**, 1851–1867, https://doi.org/10.1175/JAMC-D-12-0144.1.

Homeyer, C. R., 2014: Formation of the enhanced-V infrared cloud-top feature from high-resolution three-dimensional radar observations. *J. Atmos. Sci.*, **71**, 332–347, https://doi.org/10.1175/JAS-D-13-079.1.

——, J. D. McAuliffe, and K. M. Bedka, 2017: On the development of above-anvil cirrus plumes in extratropical convection. *J. Atmos. Sci.*, **74**, 1617–1633, https://doi.org/10.1175/JAS-D-16-0269.1.

Houser, J. L., H. B. Bluestein, and J. C. Snyder, 2015: Rapid-scan, polarimetric, Doppler radar observations of tornadogenesis and tornado dissipation in a tornadic supercell: The "El Reno, Oklahoma" storm of 24 May 2011. *Mon. Wea. Rev.*, **143**, 2685–2710, https://doi.org/10.1175/MWR-D-14-00253.1.

——, ——, and ——, 2016: A finescale radar examination of the tornadic debris signature and weak-echo reflectivity band associated with a large, violent tornado. *Mon. Wea. Rev.*, **144**, 4101–4130, https://doi.org/10.1175/MWR-D-15-0408.1.

Kennedy, A., J. M. Straka, and E. N. Rasmussen, 2007: A statistical study of the association of DRCs with supercells and tornadoes. *Wea. Forecasting*, **22**, 1191–1199, https://doi.org/10.1175/2007WAF2006095.1.

Klemp, J. B., and R. Rotunno, 1983: A study of the tornadic region within a supercell. *J. Atmos. Sci.*, **40**, 359–377, https://doi.org/10.1175/1520-0469(1983)040<0359:ASOTTR>2.0.CO;2.

Koch, S. E., and J. McCarthy, 1982: The evolution of an Oklahoma dryline. Part II: Boundary-layer forcing of mesoconvective systems. *J. Atmos. Sci.*, **39**, 237–257, https://doi.org/10.1175/1520-0469(1982)039<0237:TEOAOD>2.0.CO;2.

Kosiba, K. A., J. Wurman, Y. Richardson, P. Markowski, P. Robinson, and J. Marquis, 2013: Genesis of the Goshen County, Wyoming, tornado on 5 June 2009 during VORTEX2. *Mon. Wea. Rev.*, **141**, 1157–1181, https://doi.org/10.1175/MWR-D-12-00056.1.

Kramar, M. R., H. B. Bluestein, A. L. Pazmany, and J. D. Tuttle, 2005: The "Owl Horn" radar signature in developing Southern Plains supercells. *Mon. Wea. Rev.*, **133**, 2608–2634, https://doi.org/10.1175/MWR2992.1.

Kumjian, M. R., and A. V. Ryzhkov, 2008: Polarimetric signatures in supercell thunderstorms. *J. Appl. Meteor. Climatol.*, **47**, 1940–1961, https://doi.org/10.1175/2007JAMC1874.1.

——, ——, V. M. Melnikov, and T. J. Schuur, 2010: Rapid-scan super-resolution observations of a cyclic supercell with a dual-polarization WSR-88D. *Mon. Wea. Rev.*, **138**, 3762–3786, https://doi.org/10.1175/2010MWR3322.1.

——, A. P. Khain, N. Benmoshe, E. Ilotoviz, A. V. Ryzhkov, and V. T. J. Phillips, 2014: The anatomy and physics of Z_{DR} columns: Investigating a polarimetric radar signature with a spectral bin microphysical model. *J. Appl. Meteor. Climatol.*, **53**, 1820–1843, https://doi.org/10.1175/JAMC-D-13-0354.1.

Kurdzo, J. M., and Coauthors, 2017: Observations of severe local storms and tornadoes with the Atmospheric Imaging Radar. *Bull. Amer. Meteor. Soc.*, **98**, 915–935, https://doi.org/10.1175/BAMS-D-15-00266.1.

Lemon, L. R., and C. A. Doswell III, 1979: Severe thunderstorm evolution and mesocyclone structure as related to tornadogenesis. *Mon. Wea. Rev.*, **107**, 1184–1197, https://doi.org/10.1175/1520-0493(1979)107<1184:STEAMS>2.0.CO;2.

——, D. W. Burgess, and R. A. Brown, 1978: Tornadic storm airflow and morphology derived from single-Doppler radar measurements. *Mon. Wea. Rev.*, **106**, 48–61, https://doi.org/10.1175/1520-0493(1978)106<0048:TSAAMD>2.0.CO;2.

Lindsey, D. T., and M. J. Bunkers, 2005: Observations of a severe, left-moving supercell on 4 May 2003. *Wea. Forecasting*, **20**, 15–22, https://doi.org/10.1175/WAF-830.1.

Line, W. E., T. J. Schmit, D. T. Lindsey, and S. J. Goodman, 2016: Use of Geostationary Super Rapid Scan Satellite Imagery by the Storm Prediction Center. *Wea. Forecasting*, **31**, 483–494, https://doi.org/10.1175/WAF-D-15-0135.1.

Loney, M. L., D. S. Zrnić, J. M. Straka, and A. V. Ryzhkov, 2002: Enhanced polarimetric radar signatures above the melting level in a supercell storm. *J. Appl. Meteor.*, **41**, 1179–1194, https://doi.org/10.1175/1520-0450(2002)041<1179:EPRSAT>2.0.CO;2.

Markowski, P., and Coauthors, 2012: The pretornadic phase of the Goshen County, Wyoming, supercell of 5 June 2009 intercepted by VORTEX2. Part II: Intensification of low-level rotation. *Mon. Wea. Rev.*, **140**, 2916–2938, https://doi.org/10.1175/MWR-D-11-00337.1.

Marquis, J., Y. Richardson, J. Wurman, and P. Markowski, 2008: Single- and dual-Doppler analysis of a tornado vortex and surrounding storm scale flow in the Crowell, TX, supercell of 30 April 2000. *Mon. Wea. Rev.*, **136**, 5017–5043, https://doi.org/10.1175/2008MWR2442.1.

Mather, J. H., and J. W. Voyles, 2013: The ARM climate research facility: A review of structure and capabilities. *Bull. Amer. Meteor. Soc.*, **94**, 377–392, https://doi.org/10.1175/BAMS-D-11-00218.1.

McCann, D. W., 1983: The enhanced-V: A satellite observable severe storm signature. *Mon. Wea. Rev.*, **111**, 887–894, https://doi.org/10.1175/1520-0493(1983)111<0887:TEVASO>2.0.CO;2.

Negri, A. J., 1982: Cloud-top structure of tornadic storms on 10 April 1979 from rapid scan and stereo satellite observations. *Bull. Amer. Meteor. Soc.*, **63**, 1151–1159, https://doi.org/10.1175/1520-0477-63.10.1151.

Oye, R., C. Mueller, and S. Smith, 1995: Software for radar translation, visualization, editing, and interpolation. Preprints, *29th Conf. on Radar Meteorology*, Vail, CO, Amer. Meteor. Soc., 359–361.

Pazmany, A. L., J. B. Mead, H. B. Bluestein, J. C. Snyder, and J. B. Houser, 2013: A mobile, rapid-scanning, X-band, polarimetric (RaXPol) Doppler radar system. *J. Atmos. Oceanic Technol.*, **30**, 1398–1413, https://doi.org/10.1175/JTECH-D-12-00166.1.

Rasmussen, E. N., J. M. Straka, M. S. Gilmore, and R. Davies-Jones, 2006: A preliminary survey of rear-flank descending reflectivity cores in supercell storms. *Wea. Forecasting*, **21**, 923–938, https://doi.org/10.1175/WAF962.1.

Rinehart, R. E., 1991: *Radar for Meteorologists*. University of North Dakota, Grand Forks, 334 pp.

Rotunno, R., 2013: The fluid dynamics of tornadoes. *Annu. Rev. Fluid Mech.*, **45**, 59–84, https://doi.org/10.1146/annurev-fluid-011212-140639.

Ryzhkov, A. V., V. B. Zhuravlyov, and N. A. Rybakova, 1994: Preliminary results of X-band polarization radar studies of clouds and precipitation. *J. Atmos. Oceanic Technol.*, **11**, 132–139, https://doi.org/10.1175/1520-0426(1994)011<0132:PROXBP>2.0.CO;2.

——, S. E. Giangrande, V. M. Melnikov, and T. J. Schuur, 2005a: Calibration issues of dual-polarization radar measurements. *J. Atmos. Oceanic Technol.*, **22**, 1138–1155, https://doi.org/10.1175/JTECH1772.1.

——, T. J. Schuur, D. W. Burgess, and D. S. Zrnić, 2005b: Polarimetric tornado detection. *J. Appl. Meteor.*, **44**, 557–570, https://doi.org/10.1175/JAM2235.1.

Salazar, J. L., and Coauthors, 2019: An ultra-fast scan C-band polarimetric atmospheric imaging radar (PAIR). *2019 IEEE Int. Symp. on Phased Array Systems and Technology*, Waltham, MA, IEEE, Paper 140, 17 October.

Schenkman, A. D., M. Xue, and D. T. Dawson II, 2016: The cause of internal outflow surges in a high-resolution simulation of the 8 May 2003 Oklahoma City tornadic supercell. *J. Atmos. Sci.*, **73**, 353–370, https://doi.org/10.1175/JAS-D-15-0112.1.

Schmit, T. J., M. M. Gunshor, W. P. Menzel, J. J. Gurka, J. Li, and S. Bachmeier, 2005: Introducing the next-generation advanced baseline imager on GOES-R. *Bull. Amer. Meteor. Soc.*, **86**, 1079–1096, https://doi.org/10.1175/BAMS-86-8-1079.

——, P. Griffith, M. M. Gunshot, J. M. Daniels, S. J. Goodman, and W. J. Lebair, 2017: A closer look at the ABI on the GOES-R series. *Bull. Amer. Meteor. Soc.*, **98**, 681–698, https://doi.org/10.1175/BAMS-D-15-00230.1.

Setvak, M., K. Bedka, D. T. Lindsey, A. Sokol, Z. Charvat, J. Stastka, and P. K. Wang, 2013: A-Train observations of deep convective storm tops. *Atmos. Res.*, **123**, 229–248, https://doi.org/10.1016/j.atmosres.2012.06.020.

Skinner, P. S., C. C. Weiss, M. M. French, H. B. Bluestein, P. M. Markowski, and Y. P. Richardson, 2014: VORTEX2 observations of a low-level mesocyclone with multiple internal rear-flank downdraft momentum surges in the 18 May 2010 Dumas, Texas, supercell. *Mon. Wea. Rev.*, **142**, 2935–2960, https://doi.org/10.1175/MWR-D-13-00240.1.

Snyder, J. C., H. B. Bluestein, V. Venkatesh, and S. J. Frasier, 2013: Observations of polarimetric signatures in supercells by an X-band mobile Doppler radar. *Mon. Wea. Rev.*, **141**, 3–29, https://doi.org/10.1175/MWR-D-12-00068.1.

——, ——, D. T. Dawson II, and J. Jung, 2017: Simulations of polarimetric, X-band radar signatures in supercells. Part II: Z_{CR} columns and rings and K_{DP} columns. *J. Appl. Meteor. Climatol.*, **56**, 2001–2026, https://doi.org/10.1175/JAMC-D-16-0139.1.

Tanamachi, R. L., H. B. Bluestein, J. B. Houser, S. J. Frasier, and K. M. Hardwick, 2012: Mobile, X-band, polarimetric Doppler radar observations of the 4 May 2007 Greensburg, Kansas, tornadic supercell. *Mon. Wea. Rev.*, **140**, 2103–2125, https://doi.org/10.1175/MWR-D-11-00142.1.

Weisman, M. L., and J. B. Klemp, 1984: The structure and classification of numerically simulated convective storms in directionally varying wind shears. *Mon. Wea. Rev.*, **112**, 2479–2498, https://doi.org/10.1175/1520-0493(1984)112<2479:TSACON>2.0.CO;2.

Wicker, L. J., and R. B. Wilhelmson, 1995: Simulation and analysis of tornado development and decay within a three-dimensional supercell thunderstorm. *J. Atmos. Sci.*, **52**, 2675–2703, https://doi.org/10.1175/1520-0469(1995)052<2675:SAAOTD>2.0.CO;2.

Wienhoff, Z. B., H. B. Bluestein, L. J. Wicker, J. C. Snyder, A. Shapiro, C. K. Potvin, J. B. Houser, and D. W. Reif, 2018: Applications of a spatially variable advection correction technique for temporal correction of dual-Doppler analyses of tornadic supercells. *Mon. Wea. Rev.*, **146**, 2949–2970, https://doi.org/10.1175/MWR-D-17-0360.1.

Wurman, J., and M. Randall, 2001: An inexpensive, mobile, rapid-scan radar. Preprints, *30th Conf. on Radar Meteor.*, Munich, Germany, Amer. Meteor. Soc., P3.4, http://ams.confex.com/ams/pdfpapers/21577.pdf.

——, Y. Richardson, C. Alexander, S. Weygandt, and P. F. Zhang, 2007: Dual-Doppler and single-Doppler analysis of a tornadic storm undergoing mergers and repeated tornadogenesis. *Mon. Wea. Rev.*, **135**, 736–758, https://doi.org/10.1175/MWR3276.1.

——, K. Kosiba, P. Markowski, Y. Richardson, D. Dowell, and P. Robinson, 2010: Finescale single- and dual-Doppler analysis of tornado intensification, maintenance, and dissipation in the Orleans, Nebraska, supercell. *Mon. Wea. Rev.*, **138**, 4439–4455, https://doi.org/10.1175/2010MWR3330.1.